QSO Metal Absorption Systems at High Redshift and the Signature of Hierarchical Galaxy Formation

Michael Rauch[1,4], Martin G. Haehnelt[2],and Matthias Steinmetz[2,3]

mr@astro.caltech.edu, mhaehnelt@mpa-garching.mpg.de, msteinmetz@astro.berkeley.edu

Subject Headings: cosmology: theory, observation — galaxies: formation, evolution — intergalactic medium — quasars: absorption lines

Astrophysical Journal, Vol. 481, June 1, 1997, in press.

[1]Astronomy Department, California Institute of Technology, Pasadena, CA 91125, USA

[2]Max-Planck-Institut für Astrophysik, Postfach 1523, 85740 Garching, Germany

[3]Department of Astronomy, University of California, Berkeley, CA 94720, USA

[4]Hubble Fellow

ABSTRACT

In a hierarchical cosmogony galaxies build up by continuous merging of smaller structures. At redshift three the matter content of a typical present-day galaxy is dispersed over several individual clumps embedded in sheet-like structures, often aligned along filaments. We have used hydrodynamical simulations to investigate the spatial distribution and absorption properties of metal enriched gas in such regions of ongoing galaxy formation. The metal and hydrogen absorption features produced by the collapsing structures closely resemble observed QSO absorption systems over a wide range in HI column density. Strong CII and SiIV absorption occurs for lines-of-sight passing the densest regions close to the center of the protogalactic clumps, while CIV is a good tracer of the prominent filamentary structures and OVI becomes the strongest absorption feature for lines-of-sight passing through low-density regions far away from fully-collapsed objects. The observed column density ratios of the different ionic species at redshift three can be well reproduced if a mean metallicity [Z/H] $=-2.5$, relative abundances as found in metal-poor stars, a UV background with intensity $J_{-22} = 3$ at the Lyman limit and either a power law spectrum ($J \propto \nu^{-1.5}$) or the spectral shape proposed by Haardt & Madau (1996) are assumed. The observed scatter in [C/H] is about a magnitude larger than that in the simulations suggesting an inhomogeneous metal distribution. Observed and simulated Doppler parameter distributions of HI and CIV absorption lines are in good agreement indicating that shock heating due to gravitational collapse is a second important heating agent in addition to photoionization heating. The large velocity spreads seen in some CIV systems may be due to the occasional alignments of the observer's line-of-sight with expanding large scale filaments. Both high-ionization multi-component heavy-element absorbers and damped Lyman alpha systems can arise from groups of moderately sized protogalactic clumps ($M_{\rm baryon} \sim 10^9 M_\odot$). Recent detections of star forming galaxies at similar redshifts are consistent with this picture.

1. Introduction

Can we understand galaxy formation at high redshift studying QSO absorption systems? Lines-of-sight (LOS) to distant QSOs must frequently traverse protogalactic environments. If the gas in these regions has already experienced some metal enrichment the galaxy formation process should produce a characteristic pattern of metal absorption lines in the QSO spectrum. If we succeed in identifying the spectroscopic signature of such regions, high-resolution spectra of QSOs at high redshift should be able to yield detailed insights into the physical state of the gas in young galaxies and the gaseous reservoir from which they form. Once the observable absorption features have been related to the properties of the absorbing objects one may hope to be able to actually constrain the galaxy formation process and cosmological parameters. This paper is mostly concerned with the first aspect: what *are* absorption systems (in particular: heavy element systems) at high redshift, and can we model them realistically by adopting a specific scenario of structure formation?

QSO absorption studies provide only one-dimensional information, so observations of single LOS cannot give independently the spatial density and the size of the objects causing the absorption. Only the product of number density and cross-section is constrained. Additional information about the spatial distribution of the absorbing gas has to be sought, e.g. by the identification of heavy element absorbers with a class of galaxies whose number density is known. As Bahcall & Spitzer (1969) and Burbidge et al. (1977) pointed out, the cross section of the absorbing gas would have to be much larger than typical half-light radii of present-day spiral galaxies if these objects had the same comoving space density as such galaxies. First observational evidence in favor of large metal absorption cross-sections came from work by Bergeron (1986) who discovered low redshift galaxies close to the LOS to QSOs with known MgII absorption systems, coincident in redshift with the absorbers. Surveys of optically thick (Lyman Limit) absorption systems and galaxies at intermediate redshift have reported results consistent with galaxies being surrounded by MgII absorbing halos of radius $\sim$ 40kpc (e.g. Bergeron (1995), Steidel (1995), Churchill, Steidel & Vogt (1996)). Extending such work to optically thin systems and lower redshifts Lanzetta et al. (1995) found evidence for even larger HI halos with radii of order 160 kpc. Similarly, damped Lyα systems were interpreted by Wolfe and collaborators (e.g. Wolfe 1988, Lanzetta et al. 1991) as large protodisks, progenitors of present-day spiral galaxies with significantly larger radii at high redshift.

The large-halo/disk scenario is able to qualitatively explain the ionization and component structure of heavy element absorption systems, especially the observations of low and intermediate redshift low ionization MgII systems, and perhaps also the strong clustering measured for CIV systems (Sargent et al. 1979, Sargent, Boksenberg & Steidel 1988, Petitjean & Bergeron 1994). In this picture the individual absorption components are dense clouds pressure-confined by hot gas and orbiting in a large gravitationally bound halo or co-rotating in a disk. Such a two phase medium could be produced e.g. by thermal instability (Bahcall 1975, Fall & Rees 1985, Mo 1994). Mo & Miralda-Escudé (1996) investigated such a model in detail and found that the clouds responsible for MgII and CIV should have a typical mass $\sim 10^6 M_\odot$ and radial extent ~ 1 kpc.

At high redshift much less is known about the cross-section of metal absorbers. Secure identifications of the absorbing objects with massive galaxies are currently restricted to low redshift. Nevertheless, large virialized objects have also been invoked, mainly from a heuristic point of view, to explain some of the characteristics of *high redshift* (z> 2) absorbers (e.g. Wolfe 1988). Measurements of the sizes of damped Lyα absorbers at high redshift so far are rare and appear contradictory (e.g. Møller & Warren 1995, Djorgovski et al. 1996). *Large* disks are, however, not the only viable dynamical model for the observed velocity structure. Moreover, observations of galaxies at high redshift are strongly biased towards objects with high current star formation rates. Thus it is not clear whether the transverse separations on the sky of galaxy-absorber pairs coincident in redshift do reliably indicate the presence and sizes of any large, coherent objects. It is difficult to ascertain that there is not an undetected (not necessarily faint) galaxy closer to the LOS.

The alternative possibility of "smaller" but more numerous objects as sources of the metal absorption has also been explored earlier. Tyson (1988) suggested identifying damped Lyα systems with gas-rich dwarf galaxies instead of large proto-disks. York et al. (1986) discussed clusters of such objects to explain the component structure of CIV systems. Individual galaxy halos cannot produce potential wells deep enough to explain the largest velocity splittings of CIV systems (up to $1000\,\mathrm{km\,s^{-1}}$) as virialized motions. Pettini et al. (1983) and Morris et al. (1986) concluded that the velocity splitting and large cross-sections are equally difficult to understand if objects similar to present-day galaxy clusters placed at high redshift were causing the absorption.

Earlier attempts at understanding QSO absorption systems have mostly employed phenomenological models. The ionization state of the gas was calculated with simplified assumptions about the geometry, temperature and dynamical structure of the gas. Recently, realistic hydrodynamical simulations of the fate of gas in a universe subject to hierarchical structure formation (Cen et al. 1994, Hernquist et al. 1996) have led to a better understanding of the large scale distribution of baryons. In the new picture a coherent filamentary large scale structure of dark matter and baryons is responsible for Lyα forest absorption lines (e.g. Bi, Börner & Chu 1992; Petitjean, Mücket & Kates 1995; Zhang, Anninos & Norman 1995; Miralda-Escudé et al. 1996). Denser condensations embedded in the filaments are unstable against rapid collapse and cooling of the gas and probably form stars at their centers. In such a hierarchical picture gravitational clustering should play an increasing role in generating distinct absorption systems towards higher redshift (cf. Lake 1988). At high z typical dark matter halos are smaller and more numerous than present-day galaxies. Simple scaling laws predict that for fixed circular velocity both their mass and their radius decrease as $(1+z)^{-3/2}$ (see Kauffmann (1996) and Steinmetz (1996a) for quantitative predictions). Thus typical damped Lyα systems are predicted to be significantly smaller (rather than larger) than spiral galaxies at the present (Kauffmann 1996).

If these ideas are correct then a considerable fraction of the complexity seen in heavy element absorbers should arise from entire groups of smallish, protogalactic objects prior to merging, in addition to any structure from density variations internal to already virialized, i.e. hydrostatically or rotationally supported objects. Current observations do not yet allow us to determine what the dominant contributors to the metal absorption systems are, but they are quite consistent with this picture:

(1) Recent Keck spectroscopy of Lyα forest systems (Cowie et al. 1995, Tytler et al. 1995) has shown that contamination of Lyα forest clouds by carbon is common in high-redshift Lyα absorbers with HI column densities as low as a a few times $10^{14}\mathrm{cm}^{-2}$. In the numerical simulations such column densities typically correspond to gas densities smaller than those expected for fully collapsed objects at these redshifts (indicating baryonic overdensities of order ten), so at least some metal absorption systems may occur outside the region of full gravitational collapse.

(2) Typical observed temperatures of CIV systems are somewhat larger than expected if the gas were heated only by photoionization (Rauch et al. 1996). Such an enhancement is predicted by numerical simulations (Haehnelt, Steinmetz & Rauch 1996, hereafter paper I; Haehnelt, Rauch, Steinmetz 1996) and can be produced by shock and (to a smaller extent) adiabatic heating during the gravitational compression of the gas.

In paper I we used numerical hydrodynamical simulations to demonstrate that observed CIV absorption systems can indeed be qualitatively understood in terms of absorption by "protogalactic clumps" (PGCs), i.e., small, future constituents of large galaxies, forming through gravitational instability in a hierarchical cosmogony. These objects have large enough masses and HI column densities to have formed stars and appear as an early generation of galaxies. The CIV and HI absorption features caused by groups of PGCs were found to resemble observed CIV and HI absorption systems if an overall homogeneous abundance of [C/H] ≈ -3 to -2 was assumed.

Here, we will perform a quantitative analysis and extend the work to a larger set of diagnostically useful ionic species. Section 2 will give the details of the numerical modelling. In section 3 we discuss the line formation process and the physical nature of the absorbing structures in regions of ongoing galaxy formation. In section 4 we discuss the observational consequences. Conclusions are drawn in section 5. All analysis presented in the present paper is for simulations at $z = 3.07$.

2. Numerical simulations

2.1. The code

The simulations were performed using GRAPESPH (Steinmetz 1996b). This code combines a direct summation N-body integrator with the Smoothed Particle Hydrodynamics technique (Lucy 1977, Gingold & Monaghan 1977) and is implemented for the special purpose hardware GRAPE (Sugimoto et al. 1990). The version of the code we use here is especially adapted to follow a mixture of collisionless (dark matter) and collisional (gas) fluids. It is fully Lagrangian, three-dimensional, and highly adaptive in space and time as the result of the use of individual smoothing lengths and individual timesteps. The physical processes included in this version of the code include self-gravity, pressure gradients, hydrodynamical shocks, radiative and Compton cooling and photoheating by a UV background with a specified spectrum. We do not assume rate equilibrium for the dominant baryonic species (H, H^+, He, He^+, He^{++}, and e^-) but follow self-consistently their non-equilibrium time evolution. However, this had only modest effect on the gas temperature in the lowest density regions. The non-equilibrium time evolution can generally be neglected for the questions addressed in this paper but will be important for low column density systems at epochs close to reionization. We assume that the gas remains optically thin throughout the calculation and that the background radiation is uniform in space. Radiative transfer effects have been neglected (see also Navarro & Steinmetz 1997).

2.2. Initial conditions

The initial conditions are identical to those in Navarro and Steinmetz (1997) and were originally designed to study the formation of galaxies with circular velocities between $80\,\mathrm{km\,s^{-1}}$and $200\,\mathrm{km\,s^{-1}}$. The background cosmological model is a $\Omega = 1$, $H_0 = 50\,\mathrm{km\,s^{-1}\,Mpc^{-1}}$ cold dark matter (CDM) universe with a normalization of $\sigma_8 = 0.63$. The baryon fraction is $\Omega_b = 0.05$. Based on a P3M large scale structure simulation of collisionless dark matter in a 30 Mpc box, eight halos were selected (four each with circular velocity of about $100\,\mathrm{km\,s^{-1}}$ and $200\,\mathrm{km\,s^{-1}}$) at $z = 0$. The dark matter particles belonging to these halos are traced back from $z = 0$ to $z = 21$. The smallest spherical regions containing all the particles contributing to the future halos are then resimulated at much higher resolution. About 35000 particles are placed in spheres of radius 2.3 (3.8) Mpc (comoving) for the systems with a circular velocity of 100 km/sec (200 km/sec). The particle mass was $4.9 \times 10^6 M_\odot$ and $2.3 \times 10^7 M_\odot$ in the low- and high-mass systems, respectively. The particles within the high-resolution sphere are perturbed with the same long waves as in the original $\mathrm{P^3M}$ simulation. Additional short wavelength modes up to the Nyquist frequency of the refined particle distribution are added on a 40^3 grid with a linear extent corresponding to the diameter of the high resolution sphere. About 1200 additional particles of higher mass outside the high resolution sphere represent the tidal field of the surrounding matter. We adopt a Plummer gravitational softening of 2.5 (5) kpc for the dark matter and of 1.25 (2.5) kpc for the gas particles in the low (high) mass systems. All high resolution runs are started at $z = 21$. At smaller redshifts the high resolution region is tidally distorted. At redshift three these distortions are, however, still rather small ($\approx 10 - 20\%$ in the axis ratios).

We use several different description for the intensity, redshift dependence and frequency dependence of the UV background. Most of the simulations were done using a power-law spectral energy distribution and the redshift dependence suggested by Vedel, Hellsten & Sommer–Larsen (1994). We varied turn-on redshift, spectral index ($\alpha = 1 \ldots 2$) and normalization of the background ($J_{-22} = 0.3\ldots30$, in units of $10^{-22}\,\mathrm{erg\,s^{-1}\,cm^{-2}\,Hz^{-1}\,sr^{-1}}$). The more realistic description of the UV background proposed by Haardt & Madau (1996) was also used. Although varying the UV background had noticeable effects on the temperature and the ionization of the gas, the effects on the overall gas distribution were small. In this paper we will only briefly discuss these effects and concentrate on simulations with $\alpha = 1.5$ and $J_{-22} = 3$ for which the background was switched on at the beginning of the simulation ($z = 21$). This corresponds to a typical quasar-like spectrum and is consistent with measurements of the helium Gunn-Peterson decrement (Davidsen, Kriss & Zeng 1996). The initial gas temperature was assumed to take the value, for which photoionization heating balances the cooling due to collisional processes and Compton scattering. For simplicity, we take the gas to be homogeneously contaminated by metals (C,Si,N,O) with solar relative abundances and an absolute metallicity of 10^{-2} solar. Effects of time dependent and/or inhomogeneous chemical enrichment were neglected. Later we shall consider different total and relative metallicities and briefly discuss implications of an inhomogeneous metal contamination.

2.3. The matter and temperature distribution

Some of the simulations were run up to the present epoch. For an individual set of initial conditions, typically between one and three disk like galaxies with circular velocities between 80 and $200\,\mathrm{km\,s^{-1}}$ have formed by now. Each consists of several thousand particles. In addition, a couple of halos with smaller masses and circular velocities (about $50\,\mathrm{km\,s^{-1}}$) are present. Size, mass and circular velocities of these disks are in good agreement with observed spiral galaxies. Compared to present-day spiral galaxies, however, the disks are too concentrated. This may be an artifact due to the neglect of energy and momentum input by star formation and AGN.

Tracing the evolution of the dark matter halo of a present-day galaxy backwards in time, one finds that at $z \sim 3$ it has "split" into several progenitors separated by several hundred kpc. While the circular velocities of these progenitors are generally slightly smaller than that of the galaxy which they will later form this is not true for the most massive progenitors. These have the same or even higher circular velocities even at redshifts of three to five, although their mass might be a factor ten smaller (White & Frenk 1991, Steinmetz 1996a). The progenitors probably suffer from the same overcooling problem as their present-day counterparts. This will have small effects for intermediate column density absorbers but conclusions regarding damped Lyα absorbers should be drawn with some caution.

Figure 1 shows the column density and temperature distribution (HI weighted along the LOS) at $z = 3.07$ (bright=high column density/hot) of a typical simulation box in which three galaxies with circular velocity $v_c \sim 100\,\mathrm{km\,s^{-1}}$ have formed at redshift zero. The area shown is 700 kpc across (proper length). Individual PGCs are embedded in a filamentary network. Regions leading to a single $v_c \sim 200\,\mathrm{km\,s^{-1}}$ galaxy look similar, with individual components scattered over several hundred kpc.

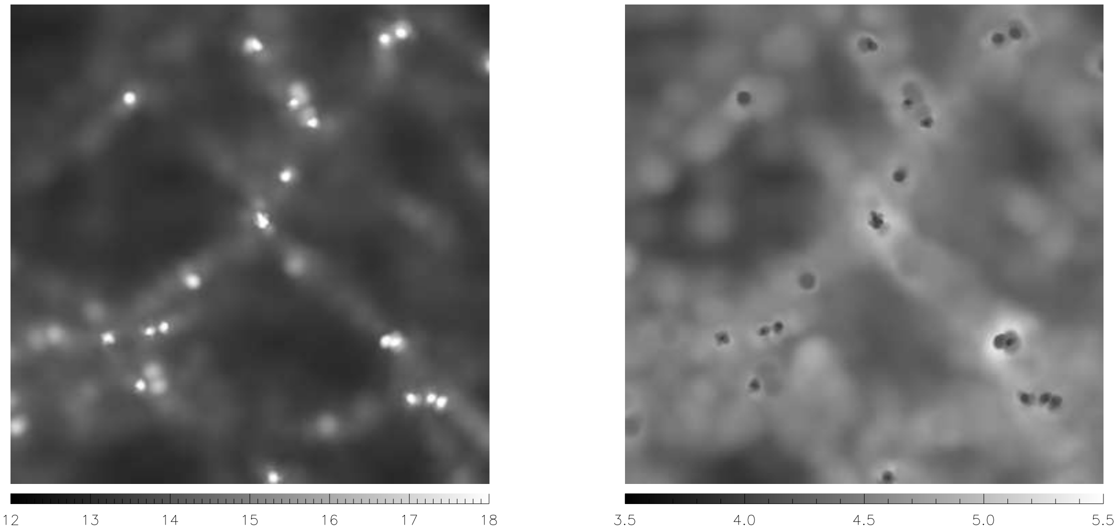

Fig. 1.— The left panel shows a grey-scale plot of the projected HI column density ($\log N$) of the inner 700 kpc of a simulation box at $z = 3.07$ which will contain three $v_c \sim 100\,\mathrm{km\,s^{-1}}$galaxies at $z = 0$. The right panel shows the temperature ($\log T$, HI column density weighted) for the same box.

The temperature in the gas rises from less than 10^4 K at the center of expansion-cooled voids (large diffuse dark areas) to a few times 10^4 K for the gas in the filaments. Higher temperatures up to several 10^5 K degrees occur in spheroidal envelopes within $\sim$ 30 kpc of the PGCs. These envelopes of hot gas arise when infalling gas is shock-heated to temperatures of the order of the virial temperature, but the density of this gas is low enough that cooling times are long compared to dynamical time scales. The temperature, the location and the mass fraction of this hot gas component can depend sensitively on the assumed spectral shape of the UV background and on the metal enrichment (Navarro & Steinmetz 1997). In the innermost few kpc of the PGCs the cooling timescales are always short compared to the dynamical time scale and the dense gas cools precipitously to temperatures below 10^4 K.

2.4. The ionization state of the gas

We have used the photoionization code CLOUDY (Ferland 1993) to calculate the ionization state of the gas for the temperature, density, and UV background of each SPH particle in the simulation. (Self-)shielding from UV radiation in optically thick regions was generally not taken into account. Thus quantitative results for LOS with column density above $10^{17}\,\mathrm{cm}^{-2}$ need to be viewed with some caution. Below we will concentrate on the ionic species HI, CII, CIV, SiIV, NV, OVI which are expected to provide some of the strongest observable lines in low and

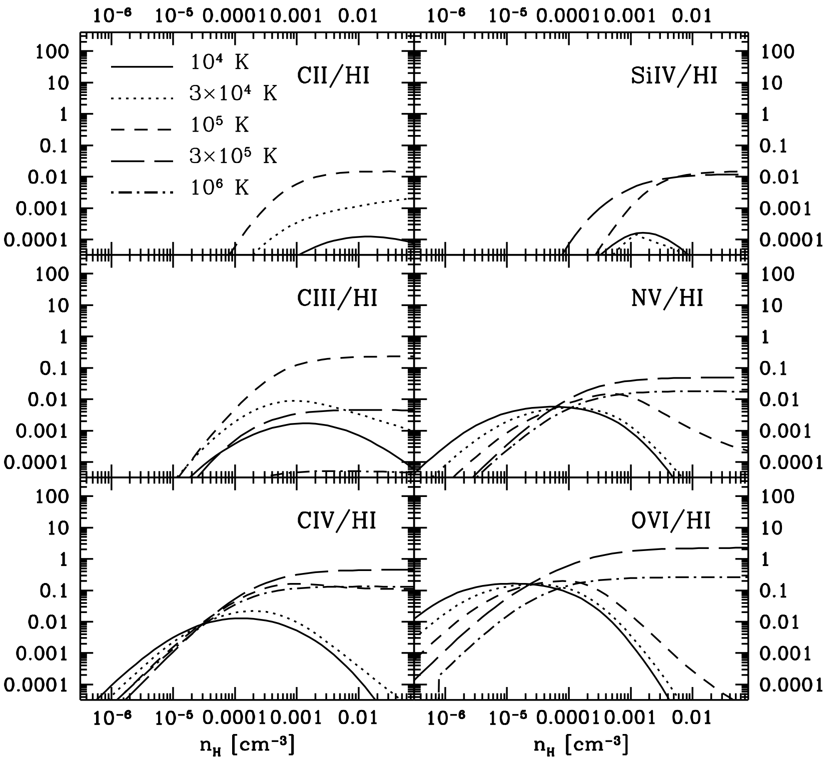

Fig. 2.— Column density ratios relative to HI for six different ionic species calculated with CLOUDY for fixed density and fixed temperatures between 10^4 K and 10^6 K as indicated on the plot. A power law with $\alpha = -1.5$ and $J_{-22} = 3$ was assumed for the background UV field.

intermediate column density absorbers. As discussed in papers I and II, observations and SPH simulations indicate that gas temperatures can significantly deviate from the equilibrium value where photo-heating balances line cooling processes. It is then important to use the actual gas temperature to calculate the ionization state of the different states. Figure 2 shows the ratios of various metal to HI column densities as a function of density for our chosen ionic species and a set of temperatures between 10^4 and 10^6 K . At high and intermediate densities the metal column density is generally increased relative to the HI column density with increasing temperature while at small densities the opposite is true. SiIV and CIV are especially temperature sensitive in the temperature and density range most relevant for intermediate column density absorption systems around $n_{\rm H} \sim 10^{-4}\,{\rm cm}^{-3}$ and $T \sim 5 \times 10^4$ K.

Figure 3 shows logarithmic column density contours for all 6 ions in steps of 1 dex. CII and SiIV are confined to dense regions marking likely sites of star formation in the center of the

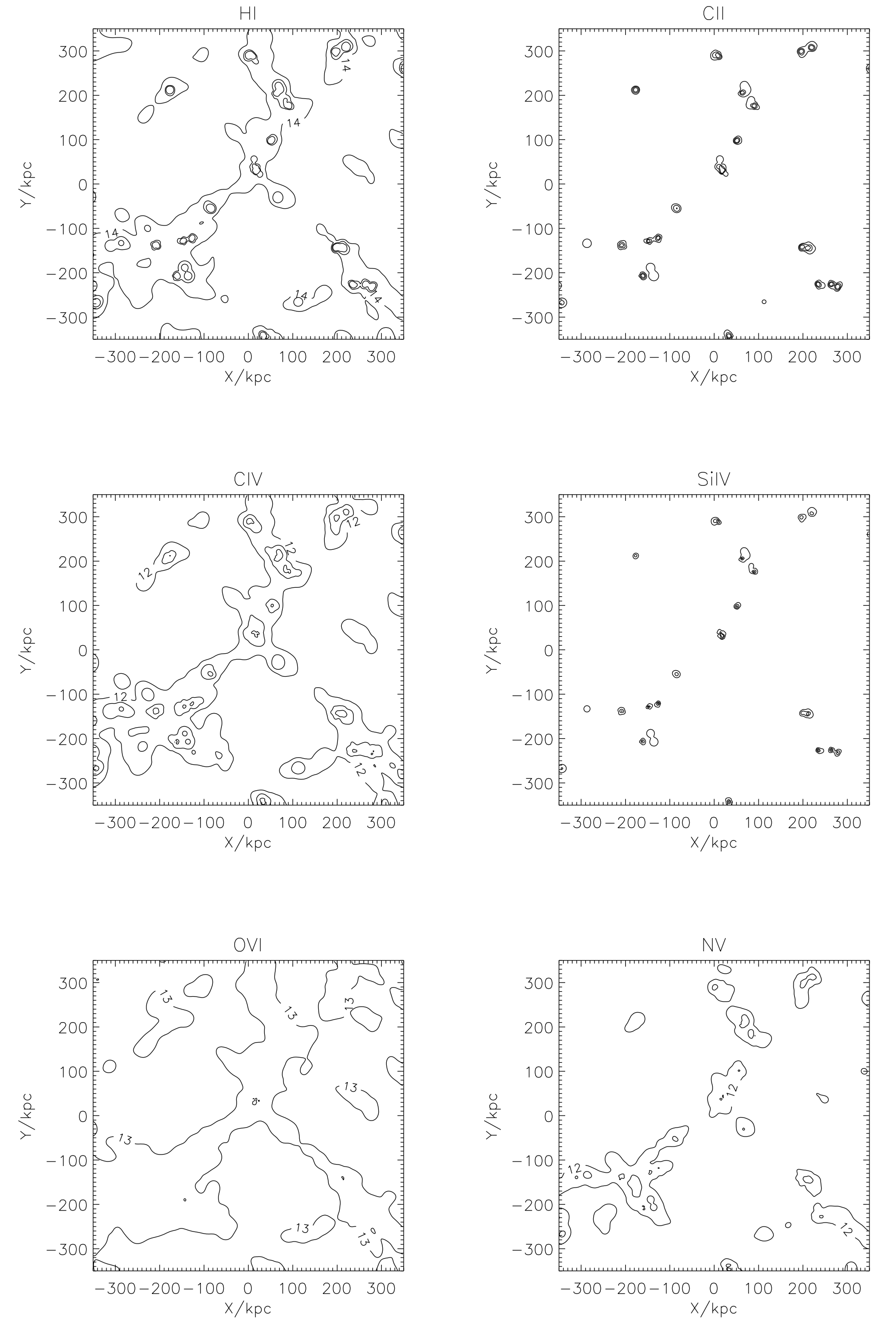

Fig. 3.— Projected column density of the inner 700 kpc of a simulation box at $z = 3.07$ which will contain three $v_c \sim 100\,\mathrm{km\,s^{-1}}$galaxies at $z = 0$. Shown are logarithmic column density contours in steps of 1 dex for HI, CII, CIV, SiIV, NV and OVI.

PGCs. C IV traces the hotter filaments and halos, while O VI matches well the low column density H I contours and traces low density gas of any temperature (cf. Chaffee et al. 1985, 1986). In the box shown the covering factor for detectable hydrogen absorption is 100%. The same is true for O VI if the metal contamination is indeed homogeneous and does not drop in regions outside the filamentary structure. Approximately one third of all LOS give detectable C IV absorption.

2.5. Generating artificial QSO spectra

To analyze the appearance of the galaxy forming region in absorption we drew 1000 LOS and generated artificial spectra for the simulation box shown in figure 1 (see section 2.3). The LOS had random orientations and random offsets within ±225 kpc from the center of the box. Optical depth $\tau(v)$ profiles along the LOS were constructed projecting the Voigt absorption line profile caused by the column density of each individual spatial pixel onto its proper position in velocity space, using the relation (for the H I Lyα line)

$$\tau(v) = \sum_i \tau_i(v - v_i) = 1.34 \times 10^{-12} \frac{\mathrm{d}N}{\mathrm{d}v}(v) \tag{1}$$

(cf. Gunn & Peterson 1965). Here $\tau_i(v - v_i)$ is the optical depth of the Voigt profile at the observed velocity v, caused by the column density ΔN_i in spatial pixel i, moving with velocity $v_i = v_{\mathrm{pec}}(i) + v_{\mathrm{Hubble}}(i)$. This can be expressed in terms of the column density per unit velocity, $\mathrm{d}N/\,\mathrm{d}v$ at v. Units of N are cm^{-2}, v is in $\mathrm{km\,s}^{-1}$.

The spectra were made to resemble typical Keck data obtainable within a few hours from a 16-17th magnitude QSO (S/N=50 per 0.043 Å pixel, FWHM = 8km/s). These "data" were then treated and analyzed in exactly the same way (by fitting Voigt profiles) as actual observations. An absorption line was deemed detectable when the equivalent width had a probability of less than 10^{-5} (corresponding to a $> 4.75\ \sigma$ event) to have been caused by a statistical fluctuation.

3. Absorption line formation in regions of ongoing gravitational collapse

Having access to the three-dimensional gas/temperature distribution and the velocity field of the gas we are able to study the line formation process as a function of the characteristic physical properties of the absorbing structures. We expect the general mechanisms to be similar to those found earlier for H I absorption features (Cen et al. 1994; Zhang et al. 1995; Hernquist et al. 1996; Miralda-Escudé et al. 1996). The emphasis of the present work is, however, on the much narrower absorption lines from metal ions. Smaller Doppler parameters and lower column densities of the heavy element lines enable us to study the velocity structure in galactic potential wells, where the corresponding H I Lyα lines are saturated and strongly blended. The resolution of the present simulations is higher than that of previous work, so we can pursue the physical quantities into regions of larger densities, and study the fate of objects of small mass.

3.1. Environments causing specific absorption patterns

The following figures illustrate a few "typical" situations where gravitational collapse gives rise to CIV and other metal absorption features. The panels give (from top to bottom) the spectra of the six ions offset vertically by 0.5 , the total baryon density, the temperature and the peculiar velocity. The x axis is the spatial coordinate along the LOS labeled by the relative velocity each position would have if following an undisturbed Hubble flow. As the structures have different sizes in position space and redshift space we decided to plot a spectral region larger than the spatial size of the box to show the fullest extent of the absorption system in velocity space. Making this particular choice creates the impression of a lack of absorption both blue and redward of the center as any absorption features created beyond the spatial boundaries of the simulated region but projected into the velocity space shown are not present. In the case of CIV, SiIV, NV, and OVI only the stronger transition of each doublet is shown. The dotted lines connect the spatial positions of overdense regions (selected manually) to their density weighted positions in velocity space.

3.1.1. Collapsing regions of moderate overdensity

Figure 4a shows a LOS producing an intermediate column density HI profile. The line is saturated but not yet damped. In LOS passing very closely to at least one PGC generally a single sharp density peak dominates the absorption line formation (see the following pictures), but more often the LOS passes through regions of smaller overdensities just about to collapse into a single object. The peculiar velocity field displays a typical infall pattern (redshift with respect to the Hubble flow for gas falling in from the front, blueshift for gas falling in from behind, a jump at the location of the density maximum). CIV and OVI are the only metals which can be detected. The absorption features are similar in appearance to the "partial Lyα limit systems" studied by Cowie et al. 1995. In this particular case the individual density peaks have converged in velocity space to form a caustic (cf. McGill 1990), but the enhanced density in physical space is still much more important for producing the absorption line (see also Miralda-Escudé et al. 1996). In principle velocity caustics may reduce the contribution of the Hubble expansion to the total velocity width of absorption lines. We find, however, that this rarely occurs. In most cases infall velocities overcompensate the Hubble flow. The ordering of two absorption lines in velocity space can even be reversed relative to their spatial positions.

3.1.2. Large velocity spread and chance alignments with filaments

Absorption caused by a chance alignment between the LOS and a filamentary structure is seen in figure 4b. The filaments generally lie at the boundaries of underdense regions ("voids") and appear to expand with velocities in excess of the Hubble flow. This is apparent from the divergent dotted lines and the ramp-like increase of the peculiar velocity as a function of real-space

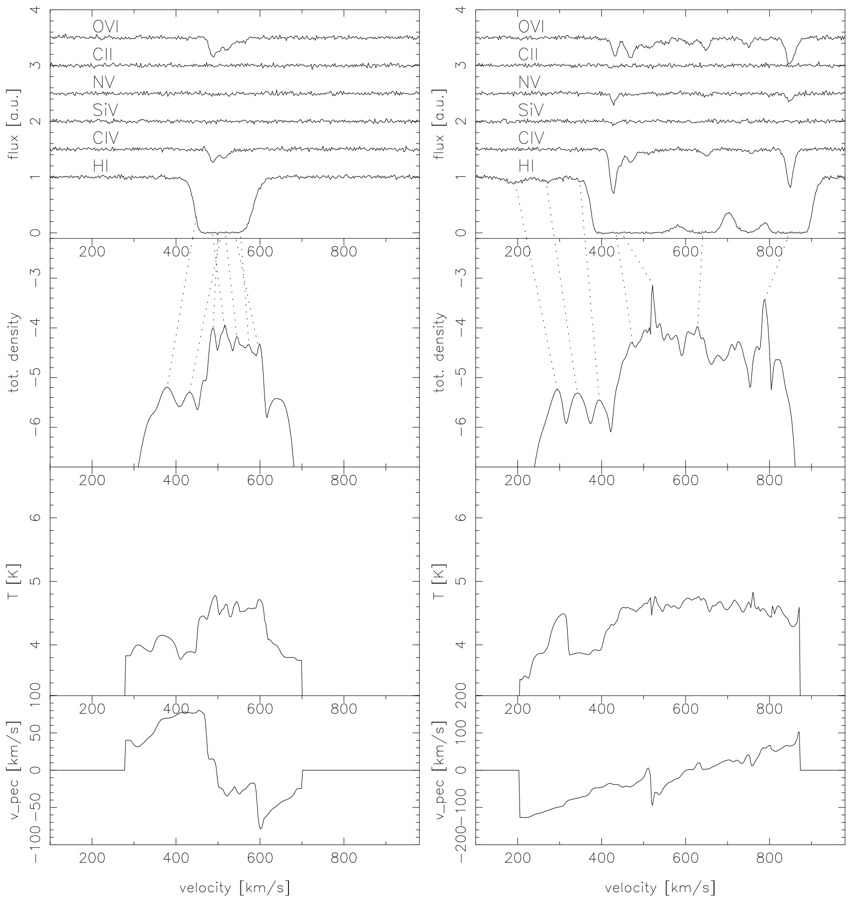

Fig. 4.— left: spectrum of a LOS through a collapsing region of moderate overdensity producing intermediate column density HI and weak CIV and OVI absorption. right: LOS along a filament apparently expanding faster than the Hubble flow. The panels give (from top to bottom) the spectra of the six ions offset vertically by 0.5, the total baryon density, the temperature and the peculiar velocity (see section 3.1). In the case of CIV, SiIV, NV, and OVI only the stronger component of each doublet is shown.

distance. Such structures rather than deep potential wells are likely to be responsible for the largest observed velocity splittings of CIV systems whereas moderate velocity splittings (up to 200 to 300 $\mathrm{km\,s^{-1}}$) are often due to a complex temperature distribution or ionization structure internal to individual PGCs (see also paper I).

3.1.3. "Damped Lyα systems"

Figure 5 shows two "damped Lyman α systems". Currently we are limited to qualitative statements about the spatial extent and ionization state of damped Lyman α systems as neither self-shielding nor energy/momentum input by star-formation or AGN have been taken into account. Nevertheless, in agreement with Katz et al. (1996) we find that for small impact parameters column densities becomes large enough to produce damped Lyα absorption lines.

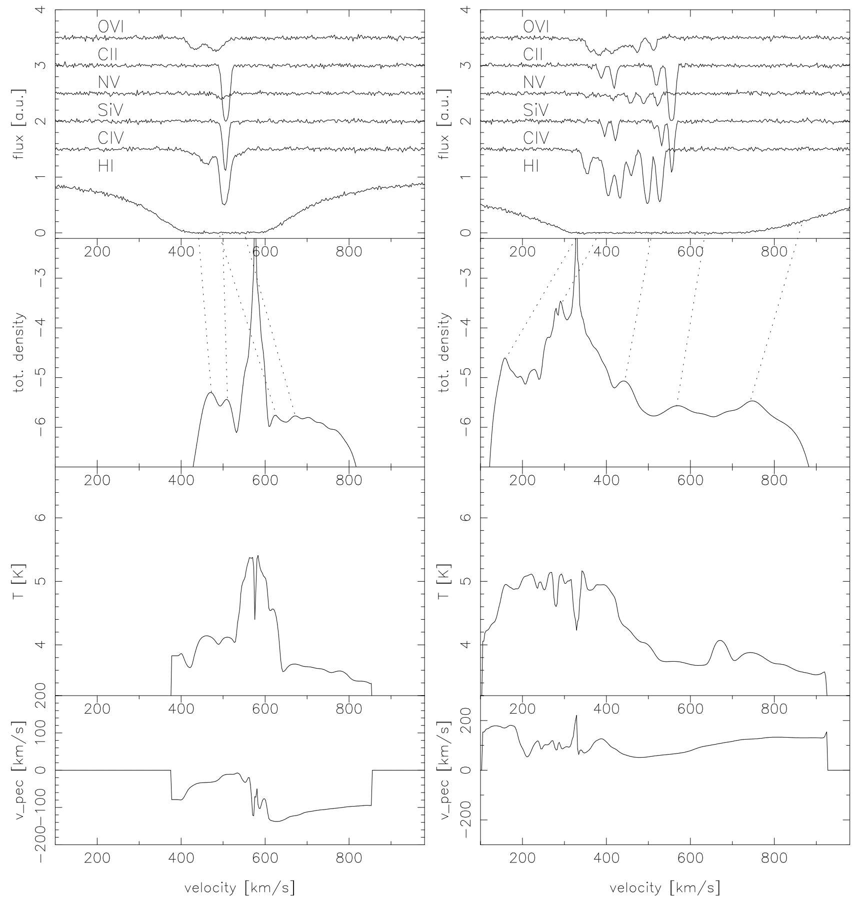

Fig. 5.— "damped Lyα systems".

Damped systems are usually dominated by one large density maximum. The density peak corresponds to a local temperature minimum due to cooling of the dense gas at the center and is surrounded by a shell of hotter infalling shock-heated gas. This leads to the characteristic double-hump structure in the temperature diagram of figure 5b. The absorption lines for the various ions of the system shown in figure 5a appear rather similar to each other in terms of position and line shape, with the exception of OVI which arises at much larger radii. In general, the maxima of the high ionization species for these highly optically thick systems need not coincide with the centers of the HI lines and those of lower ionization species. Figure 5b illustrates a situation where the component structure has a very complex origin. While the strongest CII and SiIV components coincide with the center of the damped Lyα line, the CIV and NV positions are far off, indicating differential motion between the high and low ionization regions.

It is likely that the effects of hydrodynamic and thermal instabilities and star formation will lead to substantial additional density and temperature variations on scales of kpc or less, not captured by the present simulation. We do not know how much of this structure would actually be visible in absorption, but the number of discernable absorption components seen in the simulated spectra is probably best interpreted as a lower limit to the number of components in actual data.

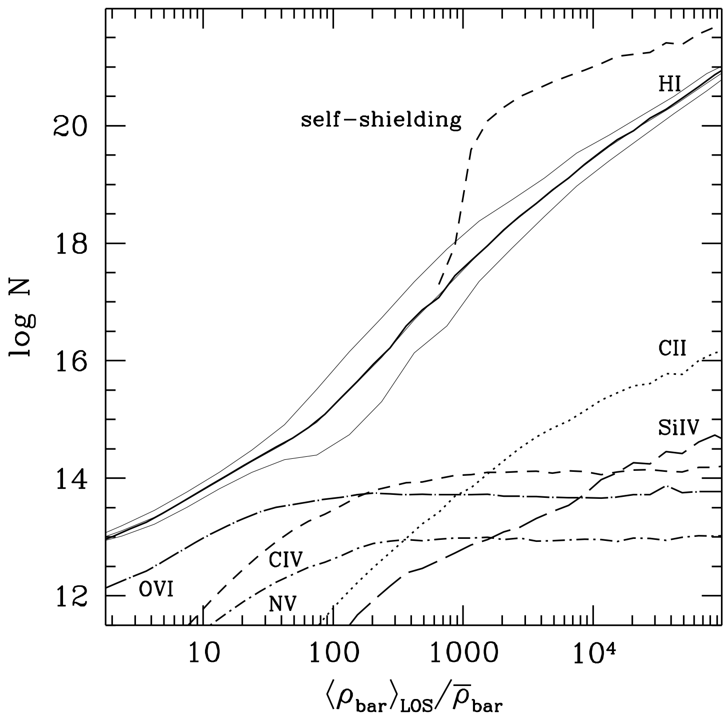

Fig. 6.— Mean (of the log) of the projected column density as a function of overdensity $\langle\rho_{\rm bar}\rangle_{\rm LOS}/\bar{\rho}_{\rm bar}$ (column density-weighted along the line-of-sight) for the simulation box shown in figure 1. For HI the thin solid lines show the $\pm1\sigma$ range in column density at fixed overdensity.

3.2. The absorption properties of individual protogalactic clumps

The solid curves in figure 6 show the good correlation between the mean log N(HI) and the baryonic overdensity in a typical simulation box. Also shown is the mean log N for our canonical set of ionic species. As expected the strength relative to HI varies considerably from species to species. CII and SiIV are strong at high HI column densities/baryonic over-densities, while CIV dominates at intermediate column densities and OVI probes the low density regime. We have also plotted a simple self-shielding correction for large HI column densities. The correction was calculated with CLOUDY specifying the total column density and mean density along the LOS.

Figure 7 shows how the spectral features change with distance from a fully collapsed clump. The plot consists of a mosaic of LOS separated by 3 kpc from each other in the x and y directions on the sky. The center of the clump is close to the top right corner. The HI Lyα line exhibits damping wings within the central $\approx$ 6 kpc.

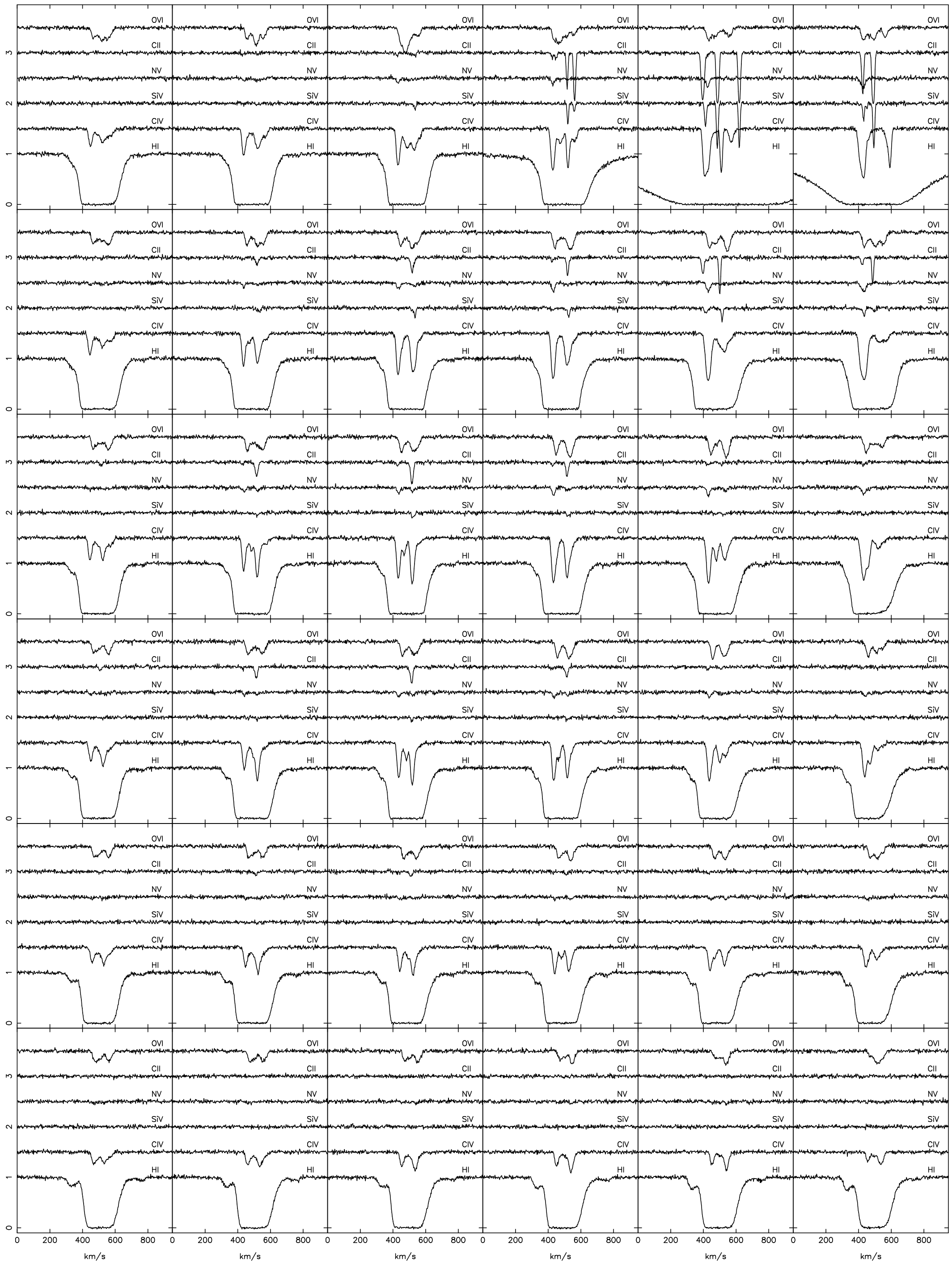

Fig. 7.— Mosaic of 6×6 lines-of-sight near a collapsed clump, separated by 3 kpc in each direction on the sky. The center of the collapsed object is close to the top right corner. The panels give the spectra of the six ions offset vertically by 0.5 for clarity. In the case of CIV, SiIV, NV, and OVI only the stronger line of each doublet is shown.

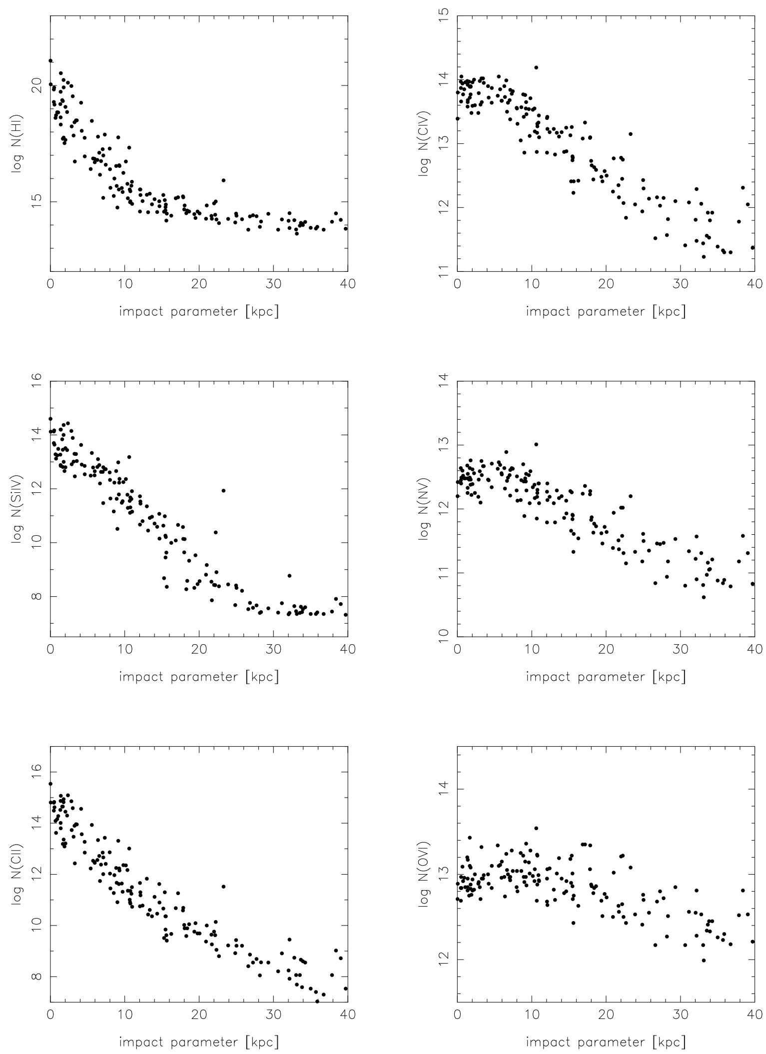

Fig. 8.— Integrated column densities along random lines-of-sight for the six ions as a function of impact parameter from the center of a protogalactic clump with $1.2 \times 10^9\,\mathrm{M}_\odot$.

To quantify the spatial coherence of the absorption properties in more detail we have investigated a set of random LOS close to a typical PGC ($M \approx 1.2 \times 10^9 \mathrm{M}_\odot$) in the simulation. Figure 8 shows the column densities as a function of impact parameter for a set of randomly oriented LOS. A sharp drop from $\log N(\mathrm{H\,I}) \geq 20$ to $\log N(\mathrm{H\,I}) \approx 15$ occurs within the first five to ten kpc. At H I column densities above $\log N \gtrsim 17$ self-shielding should become important. This will lead to an even steeper rise toward smaller radii. After the rapid drop the H I column density decreases very gradually, still exceeding $\log N(\mathrm{H\,I}) \approx 14$ at 100 kpc. The typical size of the damped region of a protogalactic clump in our simulation taking self-shielding into account should be about five kpc. However, as pointed out previously this value might increase once feedback processes are taken into account.

Currently a 10m telescope can detect H I column densities of order 10^{12} cm^{-2} which means that the detectable H I radius extends far beyond 100 kpc. The largest detectable metal absorption

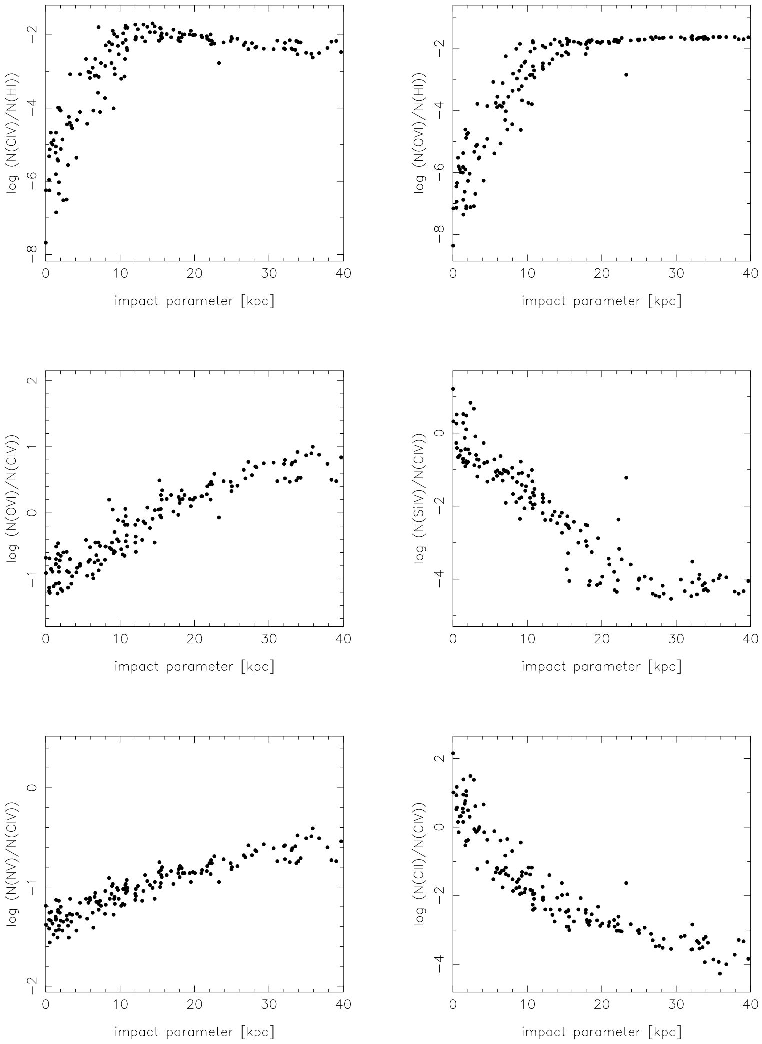

Fig. 9.— Ratios of the integrated column density along random lines-of-sight for several ions as a function of impact parameter from the center of a protogalactic clump with $1.2 \times 10^9\,\mathrm{M}_\odot$.

cross-section is subtended by CIV and probably OVI (third panel on the right); at a detection threshold of $N(\mathrm{C}\textsc{iv}) \sim 10^{12}$ cm^{-2} (realistic for very high signal-to-noise data), the radius is ~ 30 kpc; SiIV at the same significance level (taking the larger oscillator strength into account) would be detectable out to about 12 kpc. The decrease of the higher ions CIV and NV at the lowest radii is due to the increase in density; it should be even more pronounced if radiation transfer were implemented. Figure 9 gives the ratios of the LOS integrated column densities for several ions. In particular, the second panel on the left shows once more the importance of the OVI ion, which should be detectable at the largest radii with similar or even higher significance than the CIV lines. Thus, in spite of the difficulty of observing OVI in the Lyα forest the OVI/CIV column density ratio should be the best measure of the impact parameter.

4. Observational tests

4.1. Column density distributions as a test of the gas distribution and metallicities

Before discussing the overall column density distribution of HI and the metal ionic species in our simulations we stress again that our simulation boxes were not chosen randomly (see section 2.2). At our redshift of interest ($z = 3$) the mean baryonic density of the simulation boxes containing low (high) circular velocities halos is a factor 1.27 (2.97) larger than the assumed mean baryonic density of the universe for the inner 700 (proper) kpc cube. Furthermore, HI column densities projected across the simulation box are generally larger than a few times $10^{13}\mathrm{cm}^{-2}$. Below we will concentrate on properties of the four boxes containing low circular velocities halos at $z = 3.1$ for which the overdensity is moderate and which should be closest to a fair sample.

Column density distributions/ratios of ionic species with different ionization potentials are an important diagnostic of the ionization parameter, the spectral shape of the ionization field, the relative element abundances and the temperature of the gas (e.g. Bergeron & Stasinska 1986, Chaffee et al. 1986, Bechtold, Green & York 1987, Donahue & Shull 1991, Steidel 1990, Viegas & Gruenwald 1991, Ferland 1993, Savaglio et al. 1996, Songaila & Cowie 1996). In our case the distributions of densities and temperatures are predicted by the simulation (only weakly dependent on the input radiation field) so the remaining adjustable parameters are the elemental abundances and the properties of the ionizing radiation.

4.1.1. Column density distribution functions

We define the differential column density distribution as usual

$$f(N) = \frac{\mathrm{d}^2\mathcal{N}}{\mathrm{d}X\,\mathrm{d}N}, \tag{2}$$

where $\mathcal{N}$ is the number of lines and $\mathrm{d}X = (1+z)^{1/2}\,\mathrm{d}z$ (for q_0=0.5). The curves in figure 10 give $f(N)N$ at $z = 3.07$ for the four simulation boxes shifted in column density by +0.3 dex, whereas the crosses show the observed distribution (Petitjean et al. 1993). The data on the metal ions are again for a constant metallicity of [Z/H]=−2. The self-shielding correction for large HI column densities mentioned in section 3.2 is also shown. The shape of the observed distribution is matched reasonable well by the simulations once the self-shielding correction is applied. As pointed out e.g. by Hernquist et al. (1996) and Miralda-Escudé et al. (1996) the HI column density should scale with the baryon fraction, the strength of the ionizing background and the Hubble constant as $\Omega_b^2 h^3/J$. In figure 10 we got a resonably good fit for the HI column density distribution by applying a shift of +0.3 dex to the HI column density. The same shift was also applied to the metal column densities even though one should note that these depend on Ω_b and J in a more complicated way so that this might not be completely appropriate. Our "best fit" corresponds to $(\Omega_b/(0.05\,h_{50}^{-2}))^2\,/(J_{-22}\,h_{50}) \approx 0.7$, similar but slightly lower than the value found by Hernquist et

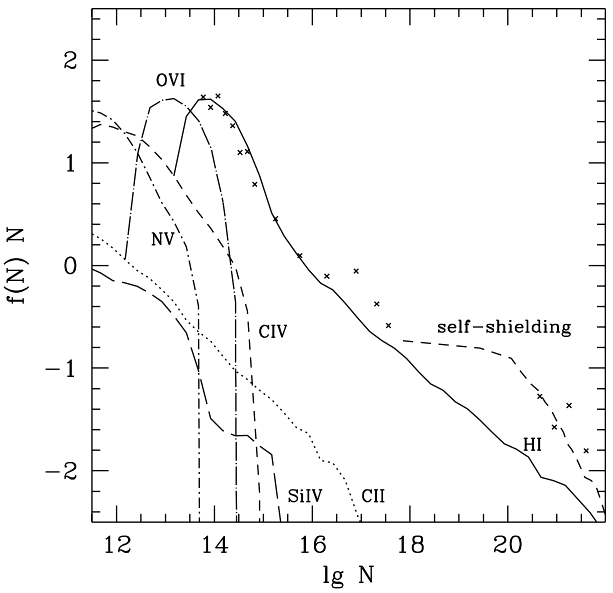

Fig. 10.— Column density distribution (f(N) N) at $z = 3$ for six different species in the simulation. Crosses show the observed column density distribution (Petitjean et al. 1993). The column density normalization is described in section 4.1.

al. (1996). Taking into account that the mean baryonic density of the volume used to calculate the column density distribution is a factor 1.27 larger then the assumed overall mean baryonic density should increase this value improving the agreement further. We do also find a deficit of systems with HI column densities around $10^{17}\,\mathrm{cm}^{-2}$, but it is smaller than the discrepancy by a factor of ten reported by Katz et al. (1996).

4.1.2. Column density ratios for random lines of sight

Figure 11 shows column density ratios for various ions, integrated along randomly offset and oriented LOS through the box described at the end of section 2.3. The most readily observable ratio is CIV/HI, which in the simulations has a maximum of about -2.2 at $N(\mathrm{HI})=10^{15}\,\mathrm{cm}^{-2}$ in the log. This is consistent with the range of values measured by Cowie et al. (1995), but a better match can be found with a carbon abundance of [C/H]= -2.5 instead of the originally adopted [C/H]= -2. At higher column densities CIV recombines to form CIII and CII with increasing density and shielding. At lower column densities CIV/HI also declines as carbon becomes more highly ionized into CV. This effect will cause difficulties for searches for carbon enrichment in the Lyα forest at column densities much lower than the presently accessible limits in HI (10^{14} cm^{-2}), as not only the HI column but also the CIV/HI ratio declines.

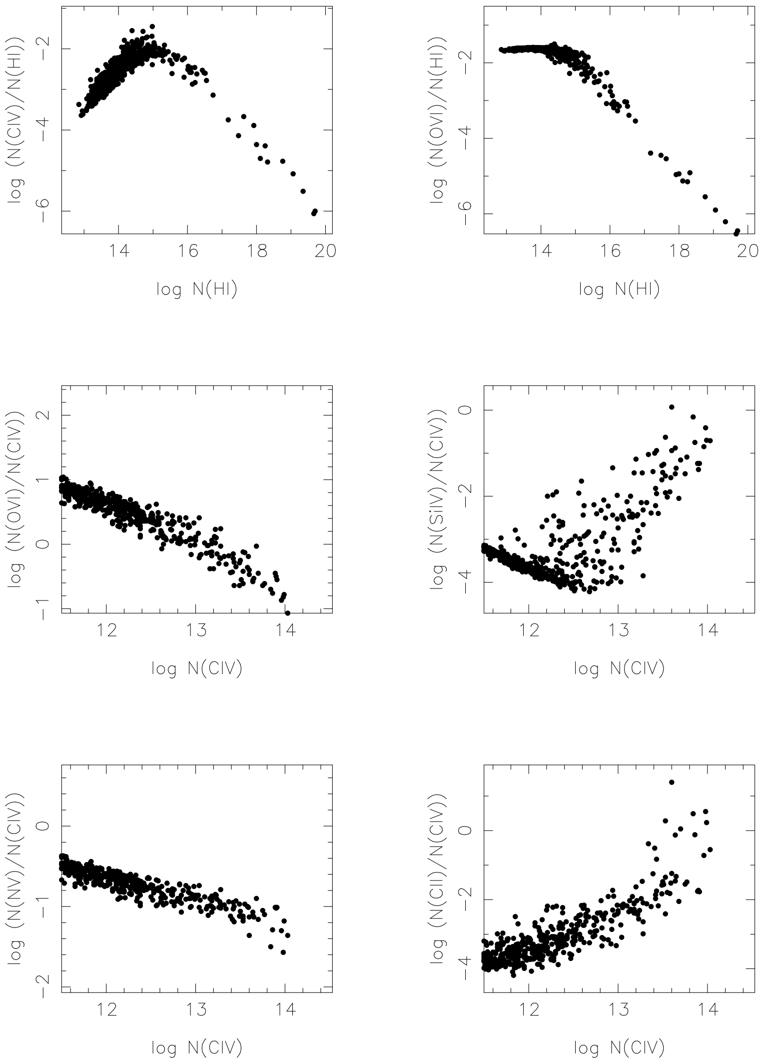

Fig. 11.— Ratios of the integrated column densities along random lines-of-sight for several ionic species as a function of HI or CIV column density.

Results obtained from Voigt profile fitting a subset of the spectra (using the software package VPFIT, Carswell et al. 1987) are shown in figure 12. Solid dots are measurements from the simulation. For comparison open boxes give observational data for CII, CIV, SiIV and NV by Songaila & Cowie (1996) and for OVI from Rauch et al. (in prep.). The circles show observational upper limits or (for OVI) indicate undetermined column densities in cases of severe blending with Lyα forest lines. The thin diagonal lines indicate the approximate detection limits for absorption features in the simulated spectra. Most of the general trends in the observed column density ratios are well reproduced. The scatter in the column density ratios between different metal ionic species is similar to that found observationally. Obviously the simulations produce a realistic range of ionization conditions.

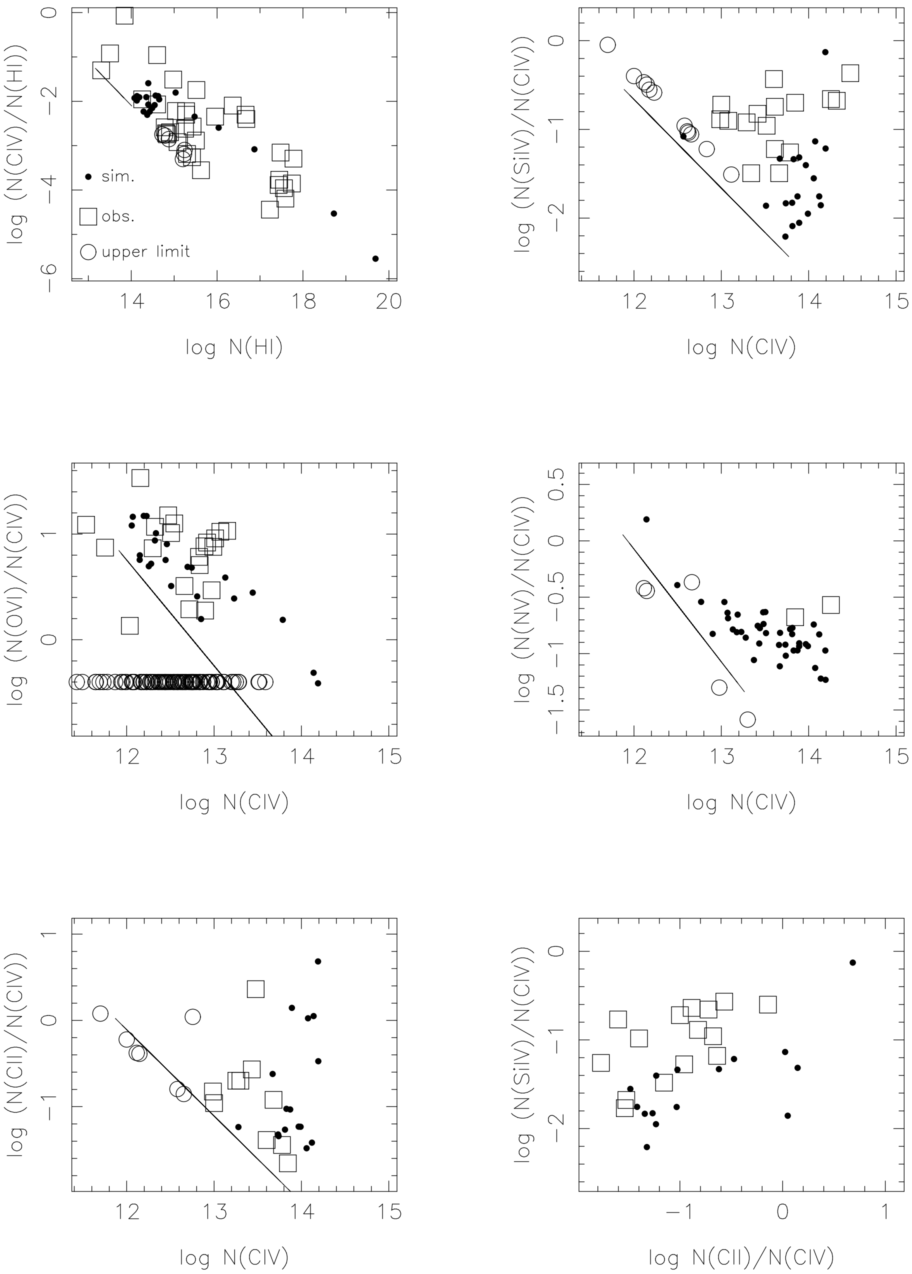

Fig. 12.— Column density ratios obtained from profile fitting the simulated data. An absolute metallicity [Z/H]$= -2$, solar relative abundances and power law UV spectrum with α=1.5 and $J_{-22} = 3$ were assumed. Filled circles denote the ratios of the sums of the column densities of all individual components along a LOS detectable at the 4.75 σ level. The thin diagonal lines give upper limits for the simulated lines in cases where only one ion (HI in the first panel and CIV in the other cases) has been detected. Open squares mark observed values (see text), open circles either observational upper limits or (bottom left panel) OVI values undetermined because of blending.

There are, however, some interesting discrepancies between simulated and actual data. First we note that the scatter in CIV/HI (panel on top left) for the observations is much larger than that in the simulations (where constant metallicity was assumed). We take this to imply that the carbon fraction and perhaps also the absolute metallicity in the outskirts of protogalactic objects at $z \sim 3$ fluctuate over one to two orders of magnitude throughout the column density range N(HI) 10^{14} to 10^{18} cm^{-2}. It is interesting to note that a similar scatter is seen in [C/Fe] in metal poor stars (McWilliam et al. 1995, Timmes, Woosley & Weaver 1995).

There are also some obvious differences between the absolute levels of the observed and simulated mean column density ratios. While the abundance ratios for the high ionization species (CIV, NV, OVI) in the simulation agree reasonably well with the observations, SiIV and CII are significantly off, with the simulated SiIV/CIV and CII/CIV ratios lower by a factor ten than the observed values.

4.1.3. Matching the observed column density ratios

Some of these discrepancies can be reduced by an appropriate modification of the relative abundances. So far we have assumed *solar relative abundances.* The generally low abundances in present-day galactic halo stars (which may contain a fossil record of the high z gas abundances) as well as optically thin CIV systems (Cowie et al. 1995) and high-redshift damped Lyα systems (Pettini et al. 1994, Lu et al. 1996) indicate that relative metal abundances like those in very metal poor stars (McWilliam et al. 1995) may be more appropriate. Below we will discuss the effect of changing the abundance pattern from solar values to: [C]=[N]=0; [Si]=[O]=0.4. The brackets denote the difference to solar abundances in dex.

Some improvement may also be expected from a different intensity or spectral shape of the ionizing radiation background. Figure 13 shows the influence of such changes on various column density ratios. The solid curve shows the values for the $\alpha = 1.5$ power law spectrum. The other curves are for several different spectral shapes and normalizations of the UV background: a power law with intensity increased and decreased by factors of 3; a spectrum taking intergalactic absorption and emission into account (Haardt & Madau 1996); and a power law with a step-shaped break at 4 Rydberg (flux reduced by a factor 100 at 4 Rydberg, constant flux for higher energies up to the point where the flux equals that of the underlying power law). The effect of the absorption edges in the Haardt & Madau spectrum on the ion ratios considered here is generally small for the relevant column densities. A power law with slope 1.5 gives a good approximation. Changing the normalization has noticeable but moderate effects on the SiIV/CIV and CII/CIV ratios. Otherwise the changes are again small. The case of a powerlaw with a 4 Ryd cutoff, however, leads to strong departures in the ion/HI, and in the ion/ion ratios for a given HI column density. A spectrum of the last kind was suggested by Songaila & Cowie (1996) and Savaglio et al. (1996) to account for large observed SiIV/CIV ratios at $z > 3$. These authors consider an increasing HeII opacity or an increasing stellar contribution to the UV background towards higher redshifts as possible causes

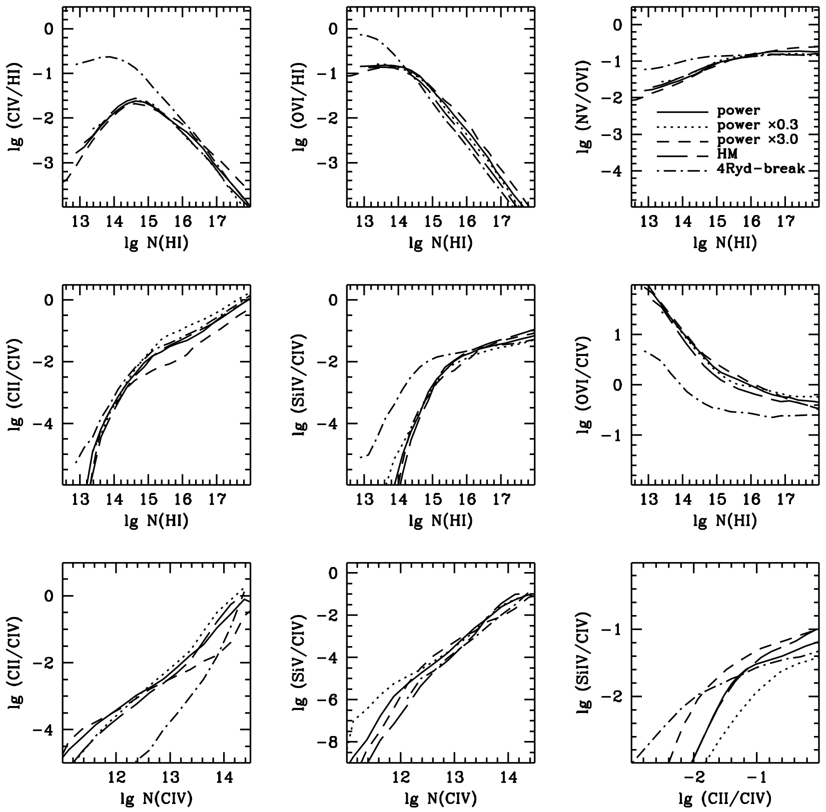

Fig. 13.— Column density ratios for various UV background radiation fields. The solid curve are for the α = 1.5 power law spectrum. The other curves are for: a power law with intensity increased and decreased by factors of 3; a spectrum taking intergalactic absorption and emission into account (Haardt & Madau 1996); and a power law with a break at 4 Rydberg (flux reduced by a factor 100 at 4 Rydberg, constant flux for higher energies up to the point where the flux equals that of the underlying power law).

for a softer spectrum.

However, for a fixed CIV column density the power law with 4 Rydberg cutoff actually even lowers the SiIV/CIV and CII/CIV ratios relative to those obtained with the originally adopted α = 1.5 power law. Moreover, such a spectrum would imply a factor three to ten smaller carbon abundance. Apparently, changing the UV radiation field does not dramatically improve the overall agreement with the observed ion ratios.

The observed and simulated column density ratios are compared in fig. 14 after adopting some of the changes discussed above (metallicity reduced by 0.5 dex to [Z/H] $=-2.5$; metal poor abundance pattern; spectrum as suggested by Haardt & Madau). The discrepancy for SiIV and CII has now been significantly reduced: the contribution to the shift in the SiIV/CIV vs. CIV came in equal parts from the adjustment in relative and absolute metallicity, whereas the CII/CIV vs. CIV ratio improved mostly because of the decrease in absolute metallicity. Thus the agreement is now quite good for SiIV, CII and CIV. OVI and NV are slightly further off but – given the large observational uncertainties in these two ions – probably consistent with the data.

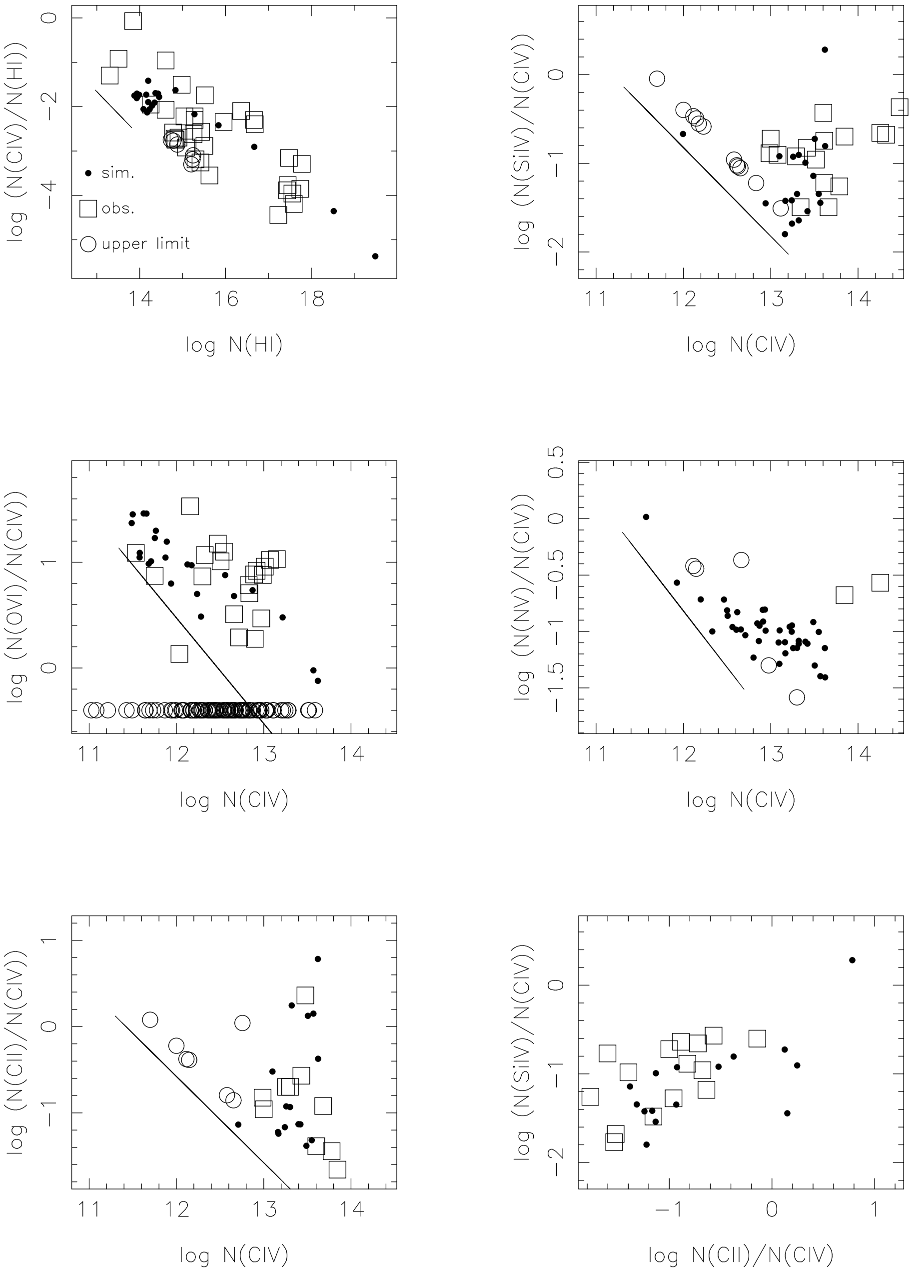

Fig. 14.— Column density ratios obtained from profile fitting the simulated data (filled circles). Compared to fig. 12 the absolute metallicity has been changed from [Z/H] = -2 to -2.5, solar relative abundances have been replaced by those of metal-poor stars ([C]=[N]=0, [Si]=[0]=0.4) and the spectrum suggested by Haardt & Madau (1996) is used instead of a power law with $\alpha = 1.5$. The diagonal lines give upper limits for the simulated absorption features in cases where only one ion (HI in the first panel and CIV in the others) has been detected. Open squares mark observed values (see text), open circles either observational upper limits or undetermined OVI .

4.2. The Doppler parameter as indicator of gas temperatures and small-scale bulk motions

Temperature and bulk velocity measurements from individual absorption lines are useful discriminants for the environment of heavy element absorption systems. The actually observable quantity is the Doppler parameter b ($=\sqrt{2}\sigma$) of the absorbing line. The line width results from a convolution of the thermal motion and the small scale bulk motion. Measurements of the Doppler parameter for ionic species with different atomic weights permit a decomposition into the contributions from thermal and non-thermal (bulk) motion. The precise nature of the decomposition depends, however, on the velocity distribution of the bulk motion.

For the simulations the relative importance of the contributions to the line formation can be easily studied as we have full knowledge of the density and peculiar velocity field along the LOS. Here we proceed as follows: from a display of the overdensity along a line of sight we choose density peaks and denote the spatial limits on both sides of the peak where the density has dropped by about an order of magnitude with a cursor. A program then computes the column density weighted temperature and RMS velocity dispersion within the selected spatial regions. Then we fit the absorption line closest to the position of the velocity centroid of the region with a Voigt profile and compare results. The top panel in figure 15 shows a plot of the "observed" CIV Doppler parameter from the fit versus the purely thermal Doppler parameter computed straight from the temperature array of the simulation. While the density weighted thermal CIV Doppler parameter of many LOS hovers around 7 to 8 $\mathrm{km\,s^{-1}}$, the "observed" values occur over a wide range. The total CIV Doppler parameter is obviously not an unbiased measure of the temperature alone, as there are substantial, varying contributions from bulk motion. It is not obvious how temperature and bulk motion should be deconvolved. Making the simplest possible ansatz of adding them in quadrature (which would be strictly true if the bulk motion followed a Gaussian velocity distribution) we arrive at the results shown in the lower panel: the observed line width does indeed measure the quadratic sum of thermal motion and RMS velocity dispersion to a reasonable accuracy. Outliers in the plot are due small spurious line components sometimes introduced by the semi-automatic fitting program VPFIT to improve the quality of the fit.

How realistic are the gas motions in the simulation? To compare the simulation to real data we chose a number of randomly selected, simulated absorption lines for Voigt profile fitting. The resulting Doppler parameter column density (b–log$N$) diagrams for CIV, OVI, and HI are shown in figure 16. The scatter plots are in very good qualitative agreement with those from observational data (e.g. Rauch et al. 1996 for CIV, Hu et al. 1995 for HI; there is no comparable information yet for OVI), as are the Doppler parameter distributions for simulated and observed CIV Doppler parameters (fig. 17). The presence of a minimum b parameter for CIV and HI and a slight increase of b_{HI} with $N(HI)$ have both been observed. This agreement also holds for the decomposition into thermal and turbulent contributions to the Doppler parameter. Both, total and thermal mean Doppler parameters are indistinguishable from the observed mean b values for HI and CIV (see table 1). The observed mean thermal CIV Doppler parameter, $\langle b\rangle_{\mathrm{therm}} = 7.2\,\mathrm{km\,s^{-1}}$corresponds to

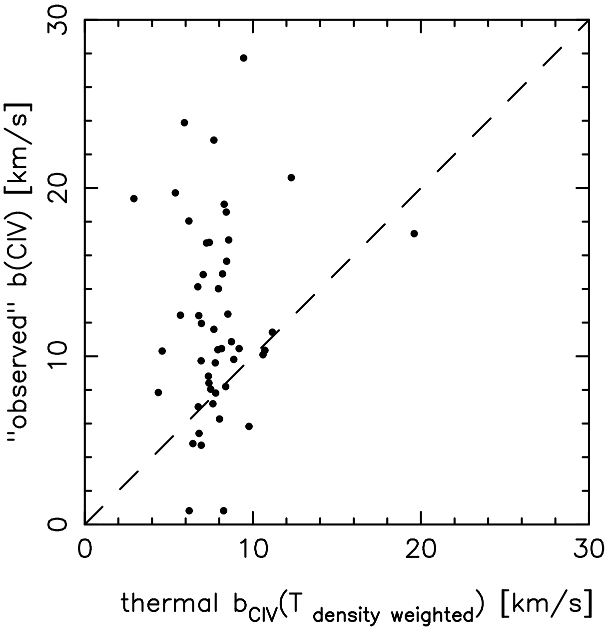

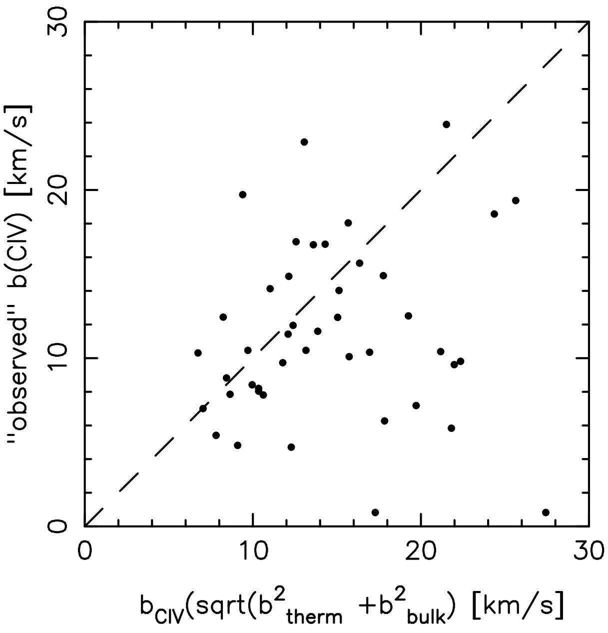

Fig. 15.— Upper panel: Total C IV Doppler parameter *measured* by profile fitting versus density weighted C IV thermal Doppler parameter computed from the gas temperature in the simulation. Lower panel: Total measured C IV Doppler parameter vs. the Doppler parameter obtained by adding RMS bulk velocity dispersion and thermal velocity dispersion in quadrature.

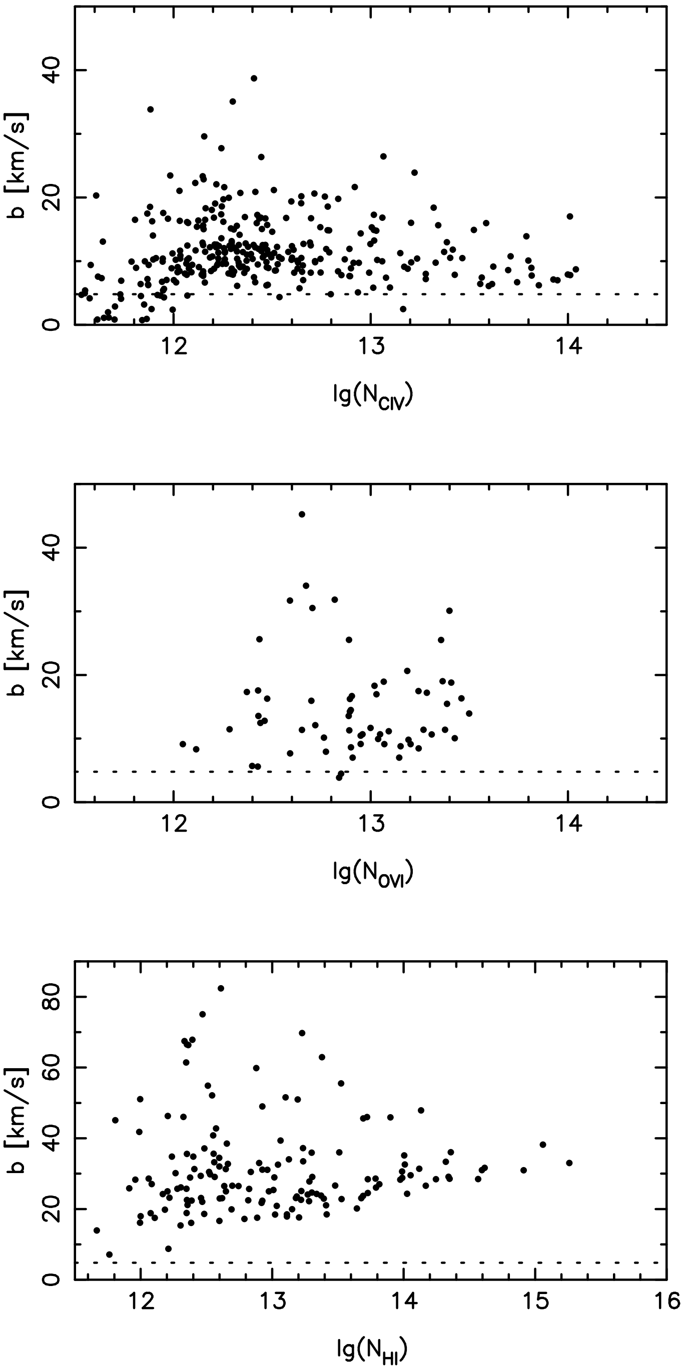

Fig. 16.— Doppler parameter – column density (b–log$N$) diagrams for CIV (top), OVI (middle) and HI (bottom). The dotted lines give the spectral velocity resolution. Note the different scales of the axes.

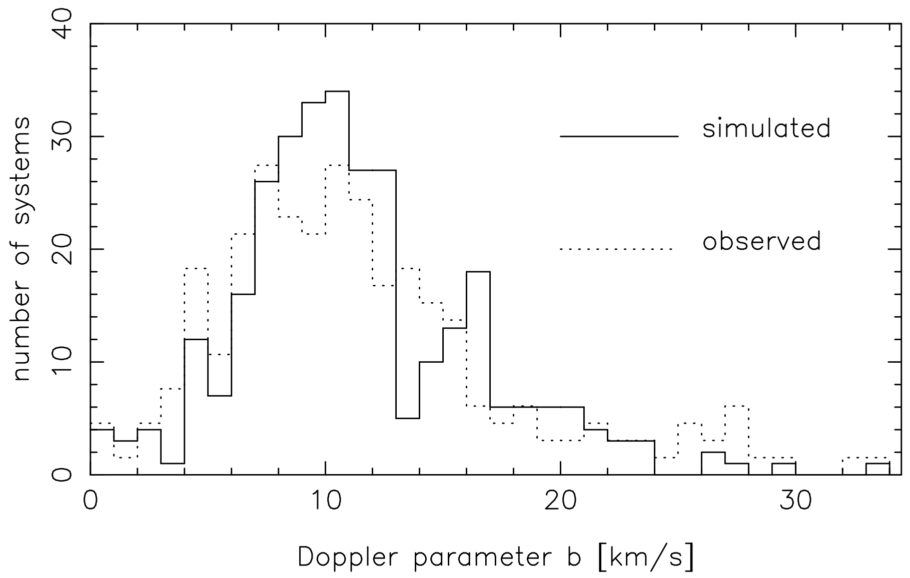

Fig. 17.— Comparison between the CIV Doppler parameters from the simulation (solid line) and the observed distribution from Rauch et al. 1996 (dotted line). The observed distribution has been scaled such as to match the total number of lines of the simulated distribution.

$\sim 4 \times 10^4$ K.

Can we observe the infalling motion during gravitational collapse directly? Naively we may expect to see substantial line broadening due to infalling gas. However, the HI density weighted velocity dispersion along the LOS (the physical quantity relevant for the line broadening) has a median as low as $11.6\,\mathrm{km\,s^{-1}}$, even though the average radius of the regions used for the computation of this quantity was as large as 40 kpc. Looking at the peculiar velocity diagrams in figures 4 and 5 with their large velocity gradients of close to $200\,\mathrm{km\,s^{-1}}$across the size of a PGC the quiescent structure may be somewhat surprising. However, the enhanced density responsible

Table 1. Observed and simulated Doppler parameters

	HI 1216 Å	CIV 1548 Å	
	$\langle b \rangle_{total}$	$\langle b \rangle_{total}$	$\langle b \rangle_{thermal}$
simulated	27.3	8.6	7.7
observed	28.0[a]	9.3[b]	7.2[b]

[a]Hu et al. 1995

[b]Rauch et al. 1996

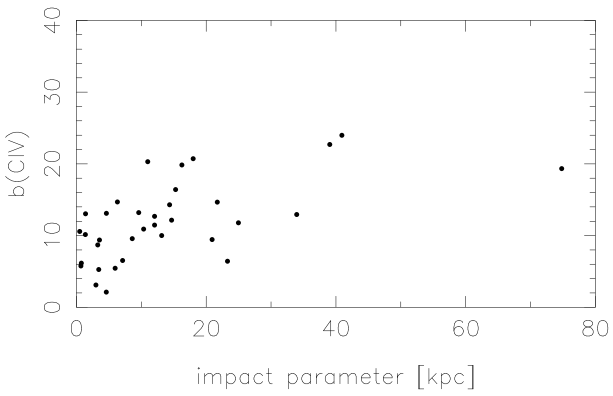

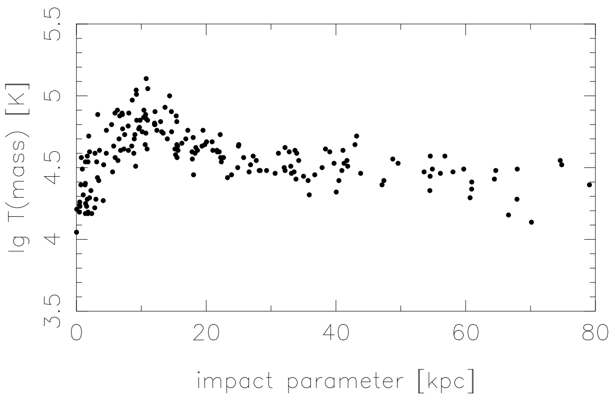

Fig. 18.— Strongest CIV Doppler parameters of each absorption complex as a function of impact parameter to the nearest PGC (top). Mass weighted temperature (bottom).

for the line formation is strongly peaked on a spatial scale much smaller than the infalling region. The line profile samples mostly the high density gas which has gone through the shock front, has cooled to temperatures of a few 10^4 K, and is more or less at rest. In principle the signature of infalling gas is still visible in the form of broad profile wings. In CIV, however, these are almost always too weak to be seen as they are due to low column density gas beyond the radius of the shock. The situation may be different for HI absorption lines (cf. Rauch 1996). In OVI with its much larger cross-section and weaker density dependence we probably also have a better chance to detect infall. The OVI Doppler parameter ($\langle b \rangle_{sim}$=11.5 km s^{-1}) is indeed higher than that of CIV, and not lower, as one could naively expect for thermally dominated gas. Obviously the OVI absorbing gas is subject to stronger non-thermal motions.

How do the Doppler parameters vary as a function of impact parameter? The LOS-integrated temperature distribution of either CIV or OVI does not show a radial variation that could be used as a measure of the impact parameter. This is due to the fact that some of the absorption components are related to different PGCs. Plotting, however, only the Doppler parameters of the strongest absorption component in each C IV complex (top panel, figure 18) we obtain a noticeable anti-correlation of b(C IV) with impact parameter from the center of the closest PGC. This seems to reflect the drop in temperature (bottom panel) and the coming to rest of the gas at small radii ($<$ 12 kpc in this case). The trend is not obvious for O VI (not shown here) which arises from a much larger region of lower density. It also does not show up in plots of b(C IV) when all components, rather than the strongest in each complex, are considered.

4.3. The two-point correlation function and the dynamical state of the absorbers on large scales

As discussed earlier the observed velocity spreads among absorption components are difficult to reconcile with an entirely dynamical velocity dispersion. In paper I it was suggested that the occasional large velocity splitting of sometimes more than $1000\,\mathrm{km\,s^{-1}}$ can be explained by chance alignments of the LOS with filaments containing several PGCs.

The TPCF for the simulation box described earlier (containing three $v_c \sim 100\,\mathrm{km\,s^{-1}}$ galaxies) is shown in the left panel of figure 19. The velocities of the C IV systems were obtained by Voigt profile fits to significant continuum depressions. The absolute normalization comes from the observed TPCF for three QSOs ($\langle z \rangle$=2.78; Rauch et al. 1996). Similar to the observed TPCF, the correlation function of C IV lines in the simulated spectra exhibits a narrow peak at the origin (the lowest velocity bin is incomplete) and a long tail out to velocities of 500-600 $\mathrm{km\,s^{-1}}$ and beyond. The overall width is somewhat smaller than that of the observed distribution. Repeating the analysis for another simulation box containing one galaxy with $v_c \sim 200\,\mathrm{km\,s^{-1}}$ we obtain the TPCF shown in the right panel of figure 19 which has much more power on large scales. Considering the rather small size of our simulation boxes, such variations from box to box are not surprising. In fact the observed TPCF is also subject to a large scatter from QSO to QSO, as some LOS often contain only one or a few systems providing large velocity splittings. It seems plausible that the observed TPCF can be explained by averaging over TPCFs from individual galaxy forming regions.

As for the origin of the large separations, splittings larger than those expected from the potential wells present ($\Delta v <$ 200-300 $\mathrm{km\,s^{-1}}$) must be due to additional contributions from large scale motions. First, there is the expansion of the filamentary structure with the Hubble flow. There will be additional streaming motions of matter towards the massive knots connecting filaments (leading to the apparent "super-Hubble" expansion seen in fig. 4b). Because of the small statistics involved, we have to await future studies to quantify the relative importance of the various effects.

As a formal measure of the velocity dispersion of an individual protogalactic region we can

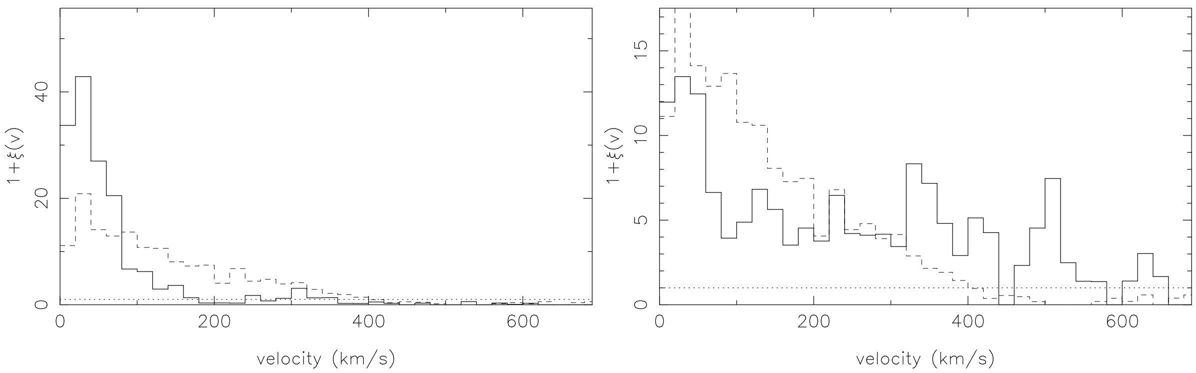

Fig. 19.— Left panel: Two-point correlation function for the CIV systems detected in a simulation box at z=3.07 (to contain three galaxies with $v_c \sim 100\,\mathrm{km\,s^{-1}}$at $z = 0$). Normalization is by the combined TPCF from the observations of three QSOs ($\langle z \rangle$=2.78; Rauch et al. 1996). Right panel: Same as above for a simulation box containing a single galaxy with $v_c \sim 200$ $\mathrm{km\,s^{-1}}$ by $z = 0$. Note the different scales of the axes.

compute the mean (over all LOS) of the RMS of the density weighted total velocity

$$\sigma_v = \left\langle \sqrt{\frac{\int (\overline{v} - v)^2 dn}{\int dn}} \right\rangle_{LOS}, \tag{3}$$

where $v = H(z)r + v_{\mathrm{pec}}$, and

$$\overline{v} = \frac{\int v dn}{\int dn}. \tag{4}$$

For the standard box, with 3 future galaxies, $\sigma_v = 100\,\mathrm{km\,s^{-1}}$. Four other boxes developing into single $\sim 200\,\mathrm{km\,s^{-1}}$ galaxies give σ_v = 142, 134, 111 and $138\,\mathrm{km\,s^{-1}}$.

4.4. Metal absorbers in emission

The observational identification of CIV absorbers at redshifts $z > 2$ with any known type of galaxies has proven difficult. Speculating that the absorbers may be related to luminous galaxies with an old population of stars Aragon-Salamanca et al. (1994) have obtained K images of QSO sight lines with known strong CIV absorbers to a K limiting magnitude of 20.3. A slight excess of objects probably at the redshift of the QSO was found but convincing identifications of individual absorbers were not possible.

Here we will briefly consider stellar population synthesis models (Bruzual & Charlot 1993, Charlot 1996) to investigate the prospects of detecting the stellar continuum from the PGCs responsible for the metal absorption systems in our model (see also Katz 1992, Steinmetz 1996a). We assume that the available gas turns into stars on time scales between 10^7 and 10^9 yr, a time span capturing the range from a short burst to extended star formation. In figure 20 the apparent

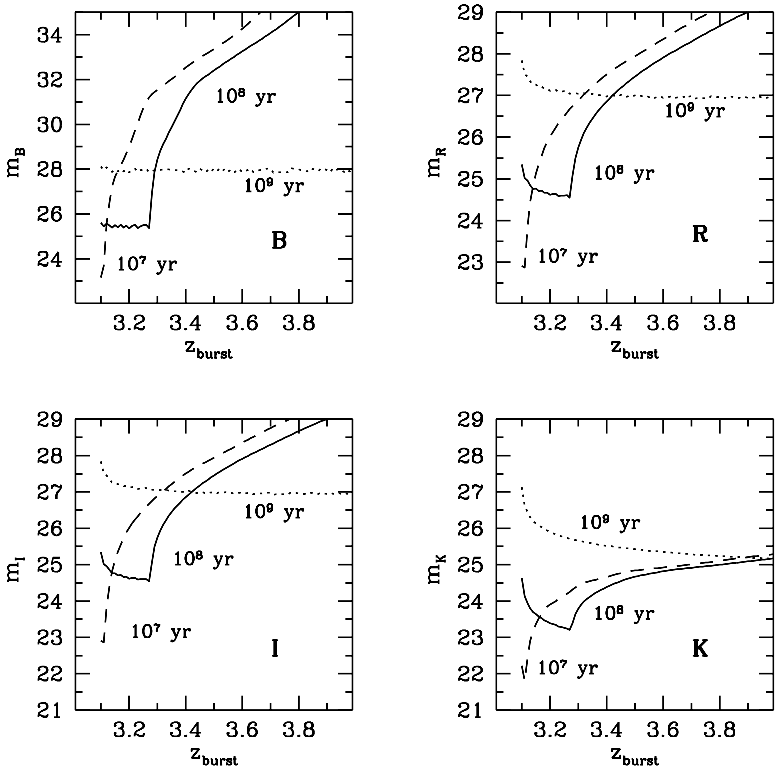

Fig. 20.— Bruzual & Charlot models for the apparent brightness (not corrected for Lyα and dust absorption, Salpeter IMF, solar metallicity) at $z = 3.1$ for a total gas mass of a protogalactic clump of $10^9\,M_\odot$, as a function of the redshift where star formation began. Different line styles indicate star formation timescales between 10^7 and 10^9 yr. Different panels are for different Johnson filters.

brightness (not corrected for Lyα and dust absorption) at $z = 3.1$ is shown for a total gas mass of $10^9\,M_\odot$(typical for a PGC) and three different star formation timescales as a function of the redshift where star formation began.

Figure 20 shows that our model would explain the non-detection of CIV absorbers in K by Aragon-Salamanca et al. (1994). Even a very short burst of $10^9\,M_\odot$reaches only a peak K magnitude of 21. Extended star formation reduces the maximum K magnitude to 25. A gas/star mass $\gtrsim 10^{11}\,M_\odot$would be necessary to be permanently detectable in K from the ground.

However, if galaxies start building up at redshifts $z \sim 3$ by merging of smaller objects recent star formation should have occurred at these redshifts. The optical passbands are then much more promising for a ground based detection of the stellar continuum. Figure 20 suggests that with HST the stellar continuum should be detectable in all wavebands redward of the Lyman break. Spectroscopic identification will only be possible for the most massive objects in the case of extended star formation, and for a fraction of bursting PGCs of average mass if the star formation timescale is short. Recently Steidel et al. (1996) and Giavalisco et al. (1996) have reported the detection of a population of star forming galaxies at comparable redshifts. It is intriguing that these objects could be identical to either a bursting fraction of average mass ($10^9\,\mathrm{M}_\odot$) objects or to the high mass end of the population of PGCs, showing extended star formation (Steinmetz 1996a).

Finally one should note that confusion with foreground galaxies is a concern when studying regions of ongoing galaxy formation as described in this paper. The inner 700 kpc of our simulation box (at z=3) shown in figures 1 and 3 correspond to an angular size slightly larger than that of an individual WFPC2 field. Thus images as large as the full Hubble deep field may be required to get a "complete" picture of the progenitors of an individual large $z = 0$ galaxy. Superposition effects are then obviously quite severe.

5. Discussion and conclusions

Gravitationally driven density fluctuations in a universe with hierarchical structure formation can explain QSO absorption phenomena at $z \sim 3$ over a wide range of column densities. While neutral hydrogen shows a rather tight correlation between column density and total density over a density range from 10^{-6} to $10^{-1}\,\mathrm{cm}^{-1}$, other ionic species probe different density and temperature regimes in a way specific to each species. The lowest H I column densities (10^{12} to $10^{14}\,\mathrm{cm}^{-2}$) arise from large-scale sheet-like density enhancements in the IGM with an overdensity of only a few compared to the mean density of the universe. In this diffuse gas (densities around $10^{-5}\,\mathrm{cm}^{-3}$) high ionization species are prevalent and O VI $\lambda1031$ is often the strongest metal absorption line. Towards higher H I column densities we start probing filaments embedded in the large-scale sheets. In these regions low column density C IV$\lambda\lambda1548, 1550$ lines from infalling gas with densities around $10^{-4}\,\mathrm{cm}^{-2}$ (overdensities of about 10 to 100) dominate the metal absorption features. C IV remains the most easily visible metal ion in the as yet unvirialized regions around the protogalactic clumps which are later to merge into present-day galaxies. Still larger H I column densities occur for lines-of-sight approaching the central regions of PGCs. These give rise to Lyman limit systems and eventually to damped Lyα absorbers. Total densities here exceed $10^{-4}\,\mathrm{cm}^{-3}$, and species like C II and Si IV become increasingly prominent. At densities above $10^{-3}\,\mathrm{cm}^{-3}$ we have reached the virialized region which is generally optically thick for radiation shortward of one Rydberg.

Although current simulations cannot precisely constrain the size of the damped region in a PGC, the fact that at $z \sim 3$ more than ten such objects exist in the comoving volume containing one $L_\star$ galaxy at $z = 0$ considerably reduces the cross section per object required to explain the observed rate of incidence of damped Lyα absorbers. If this picture is correct there should be no 1:1 correspondence between present-day galaxies and high-redshift damped (or Lyman limit) absorbers. There is then no need for hypothetical large disks/halos as high redshift progenitors of z=0 galaxies.

The analysis of artificial spectra generated from our numerical simulation was carried out using the same methods as for observational data. The results are in remarkable quantitative agreement with a number of observed properties:

The predicted shape of the HI column density distribution shows good agreement with that of the observed distribution and a good fit is obtained for $(\Omega_b/(0.05\,h_{50}^{-2}))^2/(J_{-22}\,h_{50}) \approx 0.7$. Detailed information on the strength of accompanying metal absorption has recently become available for HI column densities as small as a few times $10^{14}\,\mathrm{cm}^{-2}$. We obtain good overall agreement between the results from our artificial spectra and the observed properties, either with a simple power law UV spectrum (α=1.5, $J_{-22} = 3$) or with the spectrum proposed by Haardt & Madau (1996). This seems consistent with the lower end of the range of J values measured from the proximity effect (e.g. Giallongo et al. 1996, and refs. therein) and suggests a baryon fraction slightly exceeding the nucleosynthesis constraint (Walker et al. 1991).

The scatter of the column density ratios for SiIV/CIV, CII/CIV, and OVI/CIV versus CIV is consistent with the observational results, so the range of ionization conditions appears to be well captured by the simulations.

As already appearent from simple photoionization models the observed metal line strength corresponds to a *mean metallicity* [C/H] = −2.5 for the column density range 10^{14} to $10^{17}\,\mathrm{cm}^{-2}$. A homogeneous metal distribution reproduces the observed ion ratios well. This implies that much of the as yet unvirialized gas had been subject to a widespread phase of stellar nucleosynthesis well before redshift three, and we are seeing the infall of already metal contaminated gas. Alternatively, there may be efficient, current metal transport outward from the PGCs.

Nevertheless, the observed scatter in [C/H] is larger by a factor three to ten than predicted by our numerical simulations where the metals were distributed homogeneously. This may indicate that some of the metal enrichment took place *in situ* with incomplete mixing prior to observation. In reality there may also be a wider spread in physical conditions (e.g. spatial variations of strength and spectrum of the UV field) than assumed by the simulations.

The observed column density ratios are matched significantly better if we use relative abundances appropriate for metal-poor stars (we used [C]=[N]=0 and [Si]=[O]=0.4). Damped Lyα systems at redshifts > 3 show similar low metal abundances (−2.5 < [Z/H] < −2.0) and relative metallicities (Lu et al. 1996, and refs. therein). This is consistent with the idea that metal absorption systems at high redshift contain a record of early nucleosynthesis dominated by supernovae of type II.

The observed distribution of Doppler parameters and the relative contributions to the line width from thermal and non-thermal motion are well reproduced by the simulations. Obviously, shock heating is a second important heating agent (in addition to photoionization heating) for regions of the universe with overdensities between ten and a few hundred. Inspite of the large peculiar velocities ($\sim 100\,\mathrm{km\,s^{-1}}$) of the infalling gas CIV absorption lines are typically only $\sim$ 8 to 10 $\mathrm{km\,s^{-1}}$ wide. This is, because the CIV optical depth arises mostly in narrow post-shock regions where the shocked gas has already come to rest and is cooling rapidly. Bulk motion contributions to the Doppler parameters for OVI and HI are larger because much of the absorption arises at larger impact parameters, where infall of gas is a more important broadening agent. In the particular model of structure formation investigated here, the CIV Doppler parameter is, to a good approximation, the measure of the quadratic sum of the thermal and the RMS bulk velocity dispersion.

The large scale structure in velocity space, as measured by the CIV TPCF, is consistent with the observed CIV TPCF. This supports the hypothesis proposed in paper I that LOS which intersect expanding large scale filaments with embedded PGCs contribute significantly to the high velocity-tail of the CIV TPCF. On smaller scales ($\Delta v < 300$ kms^{-1}) we may be seeing genuine spatial clustering, the velocity dispersion internal to individual PGCs, and streaming motions within filaments. A hypothetical class of abundant, deep potential wells at high redshift may not be required.

We have discussed the prospects of detecting the stellar continuum which is expected from protogalactic clumps if at least some metal enrichment has occurred in situ. These objects should be visible at all optical wavelengths in deep images with the HST and in all optical passbands from the ground, at least longward of the Lyman break. We also suggested to interpret the Lyman break objects at redshifts around three reported by Steidel et al. (1996) in terms of the high mass end of the PGCs causing metal absorption systems or of a bursting fraction of lower mass PGCs. Prospects for identifying metal absorption systems at these redshifts are good. The best strategy seems to be a systematic search for Lyman-break objects within a few arcseconds to the line-of-sight to quasars, together with follow-up spectroscopy to the faintest possible limits. PGCs which are progenitors of a particular $z = 0$ galaxy can be scattered over several hundred kpc at $z = 3$, an area larger than the field size of the Hubble WFPC2 camera, so problems with incompleteness and foreground confusion can arise.

Substantial simplifications are present in the current work; in particular additional structure on mass scales below our resolution limit may occur. In future, a large database of metal-line ratios as a function of redshift should improve constraints on the normalization and spectrum of the UV background and allow us to distinguish between possible metal enrichment histories of the IGM. In particular, in the low density regions probed by the lowest column density Lyα absorbers, we expect OVI to be considerably stronger than CIV. Thus it may be possible to push metallicity determinations with OVI closer to truly primordial gas than is possible with CIV, despite the severe problems with identifying OVI in the Lyα forest. Another interesting case for further study is SiIV. SiIV should rapidly decrease towards low densities and a detection in low HI column density systems would indicate that the normalization and/or the spectrum of the UV background differ significantly from those we have adopted. Studying the redshift evolution of the CIV velocity space correlation function may help to test the picture of hierarchical clustering. A detection of the stellar continuum expected to be associated with metal absorption systems at kpc separations from QSO lines of sight would allow us to investigate the radial and metallicity profile of the PGCs.

In summary, we have found that high-resolution hydrodynamical simulations of galaxy forming regions can substantially aid the interpretation of the observed properties of metal absorption systems. Currently these simulations are best suited for studying regions with overdensities from ten to a few hundred. Such regions are optically thin to ionizing radiation. The good and sometimes excellent agreement of the present model with observation gives reason to believe that we have correctly identified the main mechanism underlying many of the metal absorption systems at high redshift; conversely, we may take the results presented here as an argument in favor of a hierarchical galaxy formation scenario.

6. Acknowledgments

We thank Bob Carswell and John Webb for VPFIT, and Gary Ferland for making CLOUDY available to us. Len Cowie, Limin Lu, Andy McWilliam, Wal Sargent, and Simon White have provided useful discussions and comments. We thank Jordi Miralda-Escudé for a helpful referee report. MR is grateful to NASA for support through grant HF-01075.01-94A from the Space Telescope Science Institute, which is operated by the Association of Universities for Research in Astronomy, Inc., under NASA contract NAS5-26555. Support by NATO grant CRG 950752 and the "Sonderforschungsbereich 375-95 für Astro-Teilchenphysik der Deutschen Forschungsgemeinschaft" is also gratefully acknowledged.

REFERENCES

Aragon-Salamanca, A., Ellis, R.S., Schwartzenberg, J.-M., Bergeron, J.A., 1994, ApJ, 421, 27

Bahcall, J.N., Spitzer, L. 1969, ApJ, 156, L63

Bahcall, J.N. 1975, ApJ, 200, L1

Bechtold, J., Green, R.F., and York, D.G., 1987, ApJ, 312, 50

Bergeron, J., 1986, A&A,155, L8

Bergeron, J., Stasinska, G., 1986, A&A,169, 1

Bergeron, J., 1995, in *QSO Absorption Lines*, Proc. ESO Workshop, ed. G.Meylan (Heidelberg: Springer), 127.

Bi, H.G., Börner G., Chu, Y. 1992, A&A,266, 1

Bruzual, G., Charlot, S. 1993, ApJ, 405, 538

Bond, J.R., Kofman, L., Pogosyan, D., 1996, Nat, 380, 603

Burbidge, G., O'Dell, S.L., Roberts, D.H., and Smith, H.E., 1977, ApJ, 218, 33

Carswell, R.F., Webb, J.K., Baldwin, J.A., Atwood, B., 1987, ApJ, 319, 709

Cen, R., Miralda-Escudé, J., Ostriker, J.P., Rauch, M., 1994, ApJ, 437, L9

Chaffee, F.H., Foltz, C.B., Röser, H.J., Weymann, R.J., Latham D.W., 1985, ApJ, 292, 362

Chaffee, F.H., Foltz, C.B., Bechtold,J., Weymann, R.J., 1986, ApJ, 301, 116

Charlot, S., 1996, in *From Stars to Galaxies*, ASP Conference Series Vol. 98, eds. Leitherer C., Fritze-von Alvensleben U., Huchra J., in press

Churchill, C.W., Steidel, C.C., Vogt, S.S., 1996, ApJ, 471, 164

Cowie, L.L., Songaila, A., Kim, T.-S., Hu, E. 1995, AJ, 109, 1522

Davidsen, A.F., Kriss, G.A., Zheng, W., 1996, Nat, 380, 6569

Donahue, M., Shull, J.M., 1991, ApJ, 383, 511

Djorgovski, S.G., Pahre, M.A., Bechtold, J., Elston, R. 1996, Nat, 382, 6588

Fall, S.M., Rees, M.J., 1985, ApJ, 298, 18

Ferland, G.J., 1993, University of Kentucky Department of Physics and Astronomy Internal Report

Giallongo, E., Cristiani, S., D'Odorico, S., Fontana, A., Savaglio, S.,1996, ApJ, 466, 46

Giavalisco, M., Steidel, C.C., Macchetto, D., 1996, ApJ, 470, 189

Gingold, R.A., Monaghan, J.J., 1977, MNRAS, 181, 375

Gunn, J.E., Peterson, B.A., 1965, ApJ, 142, 1633

Haehnelt, M.G., Rauch, M., Steinmetz, M., 1996, MNRAS, 283, 1055

Haehnelt, M.G., Steinmetz, M., Rauch, M. 1996, ApJ, 465, L95, (paper I)

Haardt, F., Madau, P., 1996, ApJ, 461, 20

Hernquist L., Katz, N., Weinberg, D.H., Miralda-Escudé, J., 1996, ApJ, 457, L51

Hu, E.M., Kim, T.S., Cowie, L.L., Songaila, A., Rauch, M., 1995, AJ, 110, 1543

Kauffmann, G.A.M., 1996, MNRAS, 281, 475

Katz, N., 1992, ApJ, 391, 502

Katz, N., Weinberg, D.H., Hernquist, L. Miralda-Escudé, J., 1996, ApJ, 457, L57

Lake, G., 1988, ApJ, 327, 99

Lanzetta, K.M., Wolfe, A.M., Turnshek, D.A., Lu, L. McMahon R.G. et al. 1991, ApJS, 77, 1

Lanzetta, K.M., Bowen, D.V., Tytler, D. and Webb, J.K., 1995, ApJ, 442, 538

Lu, L., Sargent, W.L.W., Barlow, T.A., Churchill, C.W., Vogt, S., ApJS, in press

Lucy, L., 1977, AJ, 82, 1013.

McGill, C., 1990, MNRAS, 242, 544

McWilliam, A., Preston, G.W., Sneden, C., Searle, L., 1995, AJ, 109, 2757

Miralda-Escudé, J., Cen, R., Ostriker, J.P., Rauch, M., 1996, ApJ, 471, 582

Mo, H.J., 1994, MNRAS, 269, p49

Mo, H.J., Miralda-Escudè, J., 1996, ApJ, 469, 589

Møller, P., Warren, S.J., 1995, in *Galaxies in the Young Universe*, eds. Hippelein, Meisenheimer & Roeser, p88

Morris, S.L., Weymann, R.J., Foltz, C.B., Turnshek, D.A., Shectman, S., Price, C., Boroson, T.A. 1986, ApJ, 310, 40

Navarro, J.F., Steinmetz, M., 1997, submitted to ApJ and preprint astro-ph/9605043

Petitjean, P., Webb, J.K., Rauch, M., Carswell, R.F., Lanzetta, K., 1993, MNRAS, 262, 499

Petitjean, P., Bergeron, J.A., 1994, A&A,283, 759

Petitjean, P., Mücket, J.P., Kates, R.E., 1995, A&A,295, L9

Pettini, M., Hunstead, R.W., Murdoch, H.S., Blades, J.C., 1983, ApJ, 273, 436

Pettini, M., Smith, L.J., Hunstead, R.W., King, D.L., 1994, ApJ, 426, 79

Rauch, M., 1996, in Bremer M.N. et al. (eds.): *"Cold Gas at High Redshift"*, 137; (Dordrecht: Kluwer)

Rauch, M., Sargent, W.L.W., Womble, D.S., Barlow, T.A., 1996, ApJ, 467, L5

Sargent, W.L.W., Young, P.J., Boksenberg, A., Carswell, R.F., Whelan, J.A.J, 1979, ApJ, 230, 49

Sargent, W.L.W., Boksenberg, A., Steidel, C.C., 1988, ApJS, 68, 539

Savaglio, S., Cristiani, S., D'Odorico, S., Fontana, A., Giallongo, E., Molaro, P., A&A, in press

Songaila, A., Cowie, L.L., 1996, AJ, 122, 335

Steidel, C.C., 1990, ApJS, 74, 37

Steidel, C.C., 1995, in *QSO Absorption Lines*, Proc. ESO Workshop, ed. G.Meylan (Heidelberg: Springer), p. 139.

Steidel, C.C., Giavalisco, M., Pettini, M., Dickinson, M., Adelberger, K.L.,1996, ApJ, 462, L17

Steinmetz, M., 1996a, to appear in *The Universe at High Redshift with VLT*, Proc. ESO Workshop, ed. Bergeron J.

Steinmetz, M., 1996b, MNRAS, 278, 1005

Sugimoto, D., Chikada, Y., Makino, J., Ito T., Ebisuzaki, T. and Umemura, M., 1990, Nat, 345, 33

Timmes, F.X., Woosley, S.E., Weaver, T.A., 1995, ApJS, 98, 617.

Tyson, N.D., 1988, ApJ, 329, L57

Tytler, D., Fan, X.-M., Burles, S., Cottrell, L., Davis, C., Kirkman, D., Zuo, L., 1995, in *QSO Absorption Lines*, Proc. ESO Workshop, ed. G.Meylan (Heidelberg: Springer), p. 289.

Vedel, H., Hellsten, U., Sommer–Larsen, J., 1994, MNRAS, 271, 743

Viegas, S.M., Gruenwald, R.B., 1991, ApJ, 377, 39

Warren, S. J. and Møller, P. (1995) In *New Light on Galaxy Evolution*, IAU Symposium 171, Heidelberg June 1995, in press

Walker, T.P., Steigman, G., Schramm, D.N., Olive, K.A., Kang, H.S, 1990, ApJ, 376, 51

White, S.D.M., Frenk, C.S., 1991, ApJ, 379, 52

Wolfe, A.M., 1988, in *QSO Absorption Line: Probing the Universe*, Proc. of the QSO Absorption Line Meeting, Baltimore, 1987, Cambridge University Press

Wolfe, A.M., 1995, in *QSO Absorption Lines*, Proc. ESO Workshop, ed. G.Meylan (Heidelberg: Springer), p. 13.

York, D.G., Dopita, M., Green, R., Bechtold, J., 1986, ApJ, 311, 610

Zhang, Y., Anninos, P., Norman, M.L., 1995, ApJ, 453, L57

This preprint was prepared with the AAS LaTeX macros v4.0.